frontiers | Frontiers in Earth Science

TYPE Original Research
PUBLISHED 01 October 2025
DOI 10.3389/feart.2025.1650076

OPEN ACCESS

EDITED BY
Hu Li,
Sichuan University of Science and Engineering, China

REVIEWED BY
Zhongnan Wang,
Research Institute of Petroleum Exploration and Development (RIPED), China
Xiaofeng Zhou,
Northeast Petroleum University, China

*CORRESPONDENCE
Mingyang Lv,
2024310054@student.cup.edu.cn
Zezhang Song,
songzz@cup.edu.cn

RECEIVED 04 July 2025
ACCEPTED 01 September 2025
PUBLISHED 01 October 2025
CORRECTED 03 November 2025

CITATION
Liao W, Zhang S, Lv M, Zhao Y, Yan H, Shi G, Nooraiepour M, Ma L, Spasennykh M and Song Z (2025) The impact of multi-cycle water invasion on underground gas storages and its controlling factors.
Front. Earth Sci. 13:1650076.
doi: 10.3389/feart.2025.1650076

The impact of multi-cycle water invasion on underground gas storages and its controlling factors

Wei Liao[1], Shijie Zhang[1], Mingyang Lv[2,3]*, Yifeng Zhao[1], Huilin Yan[2,3], Guoliang Shi[2,3], Mohammad Nooraiepour[4], Lin Ma[5], Mikhail Spasennykh[6] and Zezhang Song[2,3]*

[1]Xinjiang Oilfield Gas Storage Co., Ltd, PetroChina, Changji, China, [2]State Key Laboratory of Petroleum Resources and Engineering, China University of Petroleum (Beijing), Beijing, China, [3]College of Geosciences, China University of Petroleum (Beijing), Beijing, China, [4]Department of Geosciences, University of Oslo, Oslo, Norway, [5]Department of Chemical Engineering and Analytic Sciences, The University of Manchester, Manchester, United Kingdom, [6]Center for Petroleum Science and Engineering, Skolkovo Institute of Science and Technology, Skolkovo, Russia

Underground gas storage (UGS) facilities are essential for supply security and peak-shaving in natural gas systems, yet their sustainability is limited by an incomplete understanding of water invasion. This study examines the Hutubi UGS, the largest facility in China and the first serving the West-East Gas Pipeline II, to identify the controls of water invasion under intensive injection-withdrawal cycles. Using geological data from the second member of the Ziniquanzi Formation and multi-cycle injection-withdrawal records, we combined three-dimensional geological modeling with numerical simulation to assess aquifer energy and invasion pathways. The reservoir functions as a weak water-drive system with limited aquifer support. Water invasion is stratified and directional: high-permeability channels promote preferential migration in the western E_{1-2Z2}^{1} sub-reservoir, while localized bottom-water coning dominates in the E_{1-2Z2}^{2} sub-reservoir. Six factors act in concert to govern invasion: aquifer energy, structural boundaries, sedimentary facies, reservoir heterogeneity, physical properties, and pore structure. Together, they define a coupled mechanism that shapes the magnitude and spatial distribution of water invasion. This framework advances understanding of invasion dynamics in UGS and offers practical guidance for enhancing the long-term efficiency and sustainability of natural gas storage.

KEYWORDS

underground gas storage, aquifer energy, water invasion patterns, geological modeling, numerical simulation

1 Introduction

The transition to zero carbon, aiming to achieve global carbon neutrality, poses a significant challenge for human society. Driven by global carbon neutrality goals, the energy structure is rapidly transitioning towards low-carbon and cleaner alternatives. Natural gas, with its low carbon emissions and flexible peak-shaving capabilities, has not only become a bridging energy source between traditional fossil fuels and renewables

(Zeren and Akkuş, 2020), but also plays an increasingly critical role in maintaining supply-demand balance and ensuring stable system operation amidst the rising share of intermittent sources such as wind and solar power (Yang et al., 2024). Against this backdrop, the efficient and sustainable utilization of natural gas has emerged as a strategic priority for ensuring energy security and supporting the green transition. Underground gas storage (UGS), as essential components for resource redistribution within the natural gas industry chain, offer unique systemic value in enhancing peak-shaving capabilities, responding to extreme demand fluctuations, and improving resource utilization efficiency (Li H. T. et al., 2023) From the perspective of sustainable energy development, UGS facilities also contribute to reducing unplanned emissions and waste, lowering per-unit carbon intensity, and enabling greener and low-carbon operation across the natural gas supply chain (Pan et al., 2024). Particularly in regions dominated by renewable energy, the flexible dispatch capacity of UGS promotes coordinated operation between natural gas and renewables, thereby improving the overall sustainability and resilience of the energy system (Zou et al., 2023).

At the beginning of the 20th century, UGS was initiated in North America and Europe to meet market demand and support long-distance pipeline transmission, with the objective of ensuring safe, economic, and reliable natural gas supply (Al-Shafi et al., 2023). Since the commissioning of the first UGS in the Welland gas field (Canada) in the 1940s, the number of facilities worldwide has grown substantially. According to the International Gas Union (IGU) report, approximately 925 UGS facilities had been constructed globally, with a total working gas capacity of about $4{,}930 \times 10^8$ m^3 (Zhang et al., 2021). Of this capacity, North America accounts for 36%, Europe for 24%, the Commonwealth of Independent States for 39%, the Middle East and Asia-Pacific for 0.8%, and Latin America and the Caribbean for 0.03% (Ding, 2010). Over the past 2 decades, China has witnessed rapid growth in UGS development. By the end of 2024, a total of 38 UGS facilities had been completed, providing an effective peak-shaving working gas capacity of 26.5×10^8 m^3. Based on a national consumption of 426×10^8 m^3 in 2024, this corresponds to 6.2% of annual demand, an increase of 0.4% points from the previous year (Zheng et al., 2025). The development of Chinese UGS can be broadly divided into three stages. From 1999 to 2010, the exploratory stage, storage construction was primarily launched to support the commissioning of trunk pipeline networks, with the completion of the Dazhangtuo depleted-gas-reservoir cluster and the first salt-cavern storage at Jintan. Between 2010 and 2018, supported by national fiscal funding, the sector entered a phase of comprehensive development: CNPC completed six commercial UGS clusters, including Hutubi and Xiangguosi, while Sinopec commissioned the Wen96 facility, establishing an integrated technological framework covering site selection, drilling and completion, surface engineering, and risk management (Zheng et al., 2025). Since 2018, with UGS elevated to a national energy strategy priority, investment has been accelerated by oil companies, pipeline operators, and local governments. Large-scale storage bases with capacities exceeding 10×10^8 m^3 have been established successively in Northeast, Northwest, Central-Western, Southwest, and North China, alongside expanded deployment of salt-cavern storage. Peak-shaving capacity has thus advanced rapidly, increasing from over 10×10^8 m^3 in 2019 to 26.5×10^8 m^3 in 2024, marking the entry of China's UGS development into a new phase of rapid growth and large-scale expansion.

Depleted reservoir-based UGS is the most common and economically viable form of gas storage, with more than 400 such sites worldwide, accounting for over 75% of global UGS facilities (Ren et al., 2024). Compared to developed countries, China's UGS industry started relatively late (Zhang et al., 2017). The Hutubi UGS facility, located in the Tarim Basin, was the first large-scale UGS for China's West-East Gas Pipeline II and currently the largest UGS in China. As a vital strategic reserve and peak-shaving facility in northwest China, its stable operation is indispensable for ensuring national energy security, optimizing regional energy structures, and advancing sustainable energy system development (Zhang et al., 2020). Converted from a depleted anticlinal sandstone gas reservoir located in the northern thrust belt of the Tarim Basin, the Hutubi UGS reservoir belongs to the second member of the Paleogene Ziniquanzi Formation ($E_{1\text{-}2Z2}$), buried at depths of 3,520–3,700 m. The original reservoir pressure was 33.96 MPa, with geological reserves of 126.12×10^8 m^3 under normal temperature and pressure conditions. The gas field was in production from 1998 to 2012, during which 61.95×10^8 m^3 was extracted, resulting in a pressure decline to 16.50 MPa and a significant reduction in gas-drive capacity, indicating a transition to mid-to late-stage development. To utilize the remaining storage space effectively, the gas storage facility was constructed in 2013 with a design pressure range of 34.0–18.0 MPa and a working capacity of 45.1×10^8 m^3, making it the largest peak-shaving gas storage project in China (Tang et al., 2018). However, during UGS operation, issues such as poor injectivity and limited withdrawal efficiency were observed in some wells. These problems were primarily attributed to reservoir heterogeneity and edge-water invasion, which posed serious risks to the working gas volume and operational safety (Zhang et al., 2024). Water invasion is commonly encountered during gas reservoir development due to the hydraulic connectivity between the reservoir and underlying aquifers. The degree of water invasion depends on the volume and energy of the connected aquifer (Hu et al., 2024). Aquifer energy determines the rate and scale of water invasion, which has significant implications for long-term productivity (Han et al., 2023). While moderate invasion from low-energy aquifers can enhance reservoir pressure and support gas production (Cheng et al., 2022), aggressive invasion from high-energy aquifers can lead to rapid water coning or fingering, resulting in early water breakthrough, a sharp drop in well productivity, or even premature abandonment of wells (Han et al., 2022). The water invasion mechanisms in converted UGS reservoirs are more complex than in conventional gas fields due to three main factors: (1) aquifers formed during primary development are reactivated under cyclic high-pressure injection and withdrawal conditions; (2) intense reservoir heterogeneity causes significant variation in gas-water migration pathways; and (3) the gas-water locking effect induced by periodic injection and withdrawal leads to highly complex flow dynamics. These complications present challenges for traditional water invasion evaluation methods (Jiang et al., 2024).

Conventional evaluation methods include static (Huang et al., 2015), dynamic (Zhi et al., 2022), and numerical simulation (Huang et al., 2025a) approaches. The static volumetric method estimates aquifer volume using geometrical and petrophysical parameters but lacks accuracy due to limited

dynamic responsiveness and poor adaptability to UGS systems (Ma et al., 2023). Dynamic methods such as production performance curve analysis offer early warnings but are sensitive to pressure transmission lag in low-permeability reservoirs, often underestimating water invasion under rapid cycling (Liu et al., 2020); Material balance models assume homogeneity and steady-state aquifers, limiting their ability to capture stratified water invasion. Modified nonlinear models attempt to quantify aquifer energy using dimensionless parameters such as B, but still fail to explain gas-water locking induced by multi-cycle injection and withdrawal (Tang et al., 2014; Yao et al., 2024); Compared to traditional methods, the integration of Petrel-based 3D geological modeling with reservoir numerical simulation provides a more accurate and comprehensive approach. By combining seismic interpretation, well logging, core analysis, and production history data, high-resolution 3D geological models can be constructed. Unstructured grids are used to capture structural complexity and reservoir heterogeneity, and two-phase flow models are employed to simulate the front evolution of edge and bottom water. History matching and parameter optimization techniques enable quantitative characterization of water encroachment intensity, directionality, and sweep efficiency (Tan et al., 2025). This method excels in visualizing water invasion dynamics under multi-factor coupling. It accurately reveals how faults, unconformities, and anisotropy affect water movement and identifies preferential flow channels. When combined with uncertainty quantification, it supports multi-dimensional decision-making for water invasion risk assessment and operational optimization, making it highly suitable for studying water invasion mechanisms in converted UGS systems (Liu Z. L. et al., 2023; Huang et al., 2025b).

The characteristics of water invasion in gas reservoirs essentially reflect the coupled effects of reservoir geological attributes, fluid dynamic responses, and engineering disturbances, with mechanisms that are both highly complex and strongly region-specific (Li et al., 2022). Structural configuration governs the spatial arrangement of the gas-water system and the distribution of potential energy gradients, thereby determining preferential invasion pathways (Chen et al., 2024). Physical simulation experiments by Liu et al. (Liu Q. M. et al., 2023) demonstrated that gas-water distribution is primarily controlled by the development of structural fractures, with fracture connectivity and geometry exerting a direct influence on invasion rate and trajectory. Variations in sedimentary facies dictate reservoir connectivity and flow path architecture, constraining the expansion pattern of the invasion front (Li Y. D. et al., 2023). Reservoir heterogeneity induces permeability contrasts, which in turn generate pronounced lateral and vertical differences in invasion velocity and sweep efficiency (Hu et al., 2021; Chen et al., 2021). Li et al. (Li et al., 2019) further revealed the coupled influence of petrophysical properties and heterogeneity on the degree of invasion. At finer scales, pore structure modulates two-phase flow thresholds and residual gas distribution through the interplay of capillary and viscous forces (Song et al., 2024; Mao et al., 2024). Holtz (Holtz and Major, 2004) observed that with decreasing initial gas saturation, pore structure become more complex, with reduced porosity and narrower pore throats, resulting in elevated residual gas saturation. To probe the role of pore-throat geometry, researchers have employed laser-etched micromodels to conduct waterflooding experiments, which showed that gas bubbles undergo four distinct stages, immobilization, mobilization, trapping, and rupture (Keelan, 1976), while fractured reservoirs exhibit pronounced discontinuous flow (Agarwal, 1967). During water-driven gas displacement, multiple forms of trapped gas are generated, including viscous fingering, snap-off, blind-pore entrapment, and water-blocking effects, all of which diminish gas mobility (Han et al., 2023). In addition, engineering disturbances are a critical factor. Jiang et al. (2024), using micro-visualization and microfluidic models, conducted injection–withdrawal experiments on aquifer-influenced UGS systems and found that injection-production rates exert a strong control on pore-space utilization and flow-path evolution. Excessively rapid cycling intensified gas-water interlocking and aggravated the loss of effective storage space. In summary, water invasion is governed by the synergistic interaction of structural configuration, facies distribution, heterogeneity, pore-throat characteristics, and engineering operations. Elucidating the dynamic coupling among these factors is essential for accurately predicting invasion behavior, optimizing injection-production strategies, and developing targeted water-control measures.

This study focuses on the second member of the Ziniquanzi Formation at the Hutubi UGS in the Tarim Basin. Through physical property testing, thin-section analysis, and XRD measurements, both qualitative and quantitative characterizations of reservoir petrophysics and pore structure are conducted. Calibrated log curves using core data provide insight into the distribution of sand bodies, petrophysical parameters, and heterogeneity at the reservoir scale. A comprehensive evaluation integrating volumetric, material balance, production performance, and numerical simulation methods is used to characterize aquifer energy and water invasion patterns during both production and storage phases. Finally, the study examines how structural configuration, depositional setting, and reservoir characteristics—at both macro and micro scales—influence water invasion. The findings provide theoretical support and practical guidance for improving operational efficiency, enhancing sustainable natural gas utilization, and extending the life cycle of gas storage facilities.

2 Geologic background

The Hutubi anticline is situated at the eastern end of the third structural belt within the foreland depression of the northern Tianshan (Shi et al., 2012). It was formed under the compressional stress regime of the Himalayan orogeny and developed into a faulted anticline with a near east-west-trending long axis. The structure extends approximately 20 km in length and 3.5 km in width, characterized by a central uplift with gently dipping flanks and locally superimposed minor nose-like features (Figure 1). The northern and southern limbs show contrasting dips, with the downthrown block exhibiting gentler angles and the upthrown block steeper ones, giving the structure an asymmetric geometry that is broader to the west and narrower to the east. Structural culminations are mainly located between wells HU2006 and HU 2004, as well as near well HU003 (Figure 1). The Hutubi Fault is the most prominent reverse fault in the area, with an extension of about 20 km and a throw ranging from 60 to 200 m. West of well HU2, the fault bifurcates and subdivides the anticline into upper and lower faulted segments. The downthrown block preserves a relatively complete

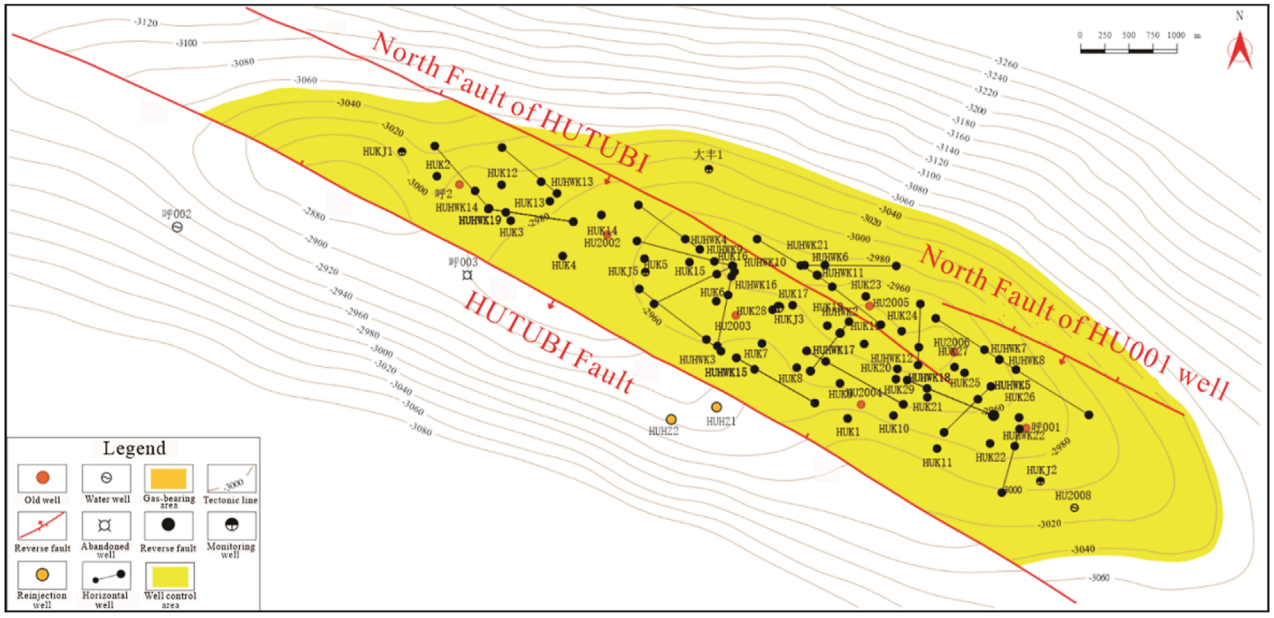

FIGURE 1
Geologic background of the research area.

geometry, transitioning from a fault nose into a full anticline, whereas the upthrown block exhibits the reverse pattern, evolving from an anticline into a fault nose. In addition to the Hutubi Fault, multiple near east-west-trending, south-dipping reverse faults are developed within the Ziniquanzi Formation. Among these, the Hutubi North Fault and the HU001 North Fault penetrate the target strata and exert a significant influence on reservoir distribution and trap integrity. Overall, this structural configuration ensures effective trapping conditions and underpins the stability of the gas reservoir for UGS operations.

From bottom to top, the stratigraphic succession of the Hutubi anticline consists of the Upper Cretaceous Donggou Formation (K_2d), the Paleogene Ziniquanzi ($E_{1\text{-}2}z$) and Anjihaihe ($E_{2\text{-}3}a$) Formations, the Neogene Shawan (N_1s), Taxihe (N_1t), and Dushanzi (N_2d) Formations, and Quaternary (Q) deposits. The total sedimentary thickness is about 1,150 m. Among these units, the Ziniquanzi Formation is the primary reservoir in the study area. It represents braided river delta-front deposits, with typical depositional microfacies including subaqueous distributary channels and interdistributary bay deposits, delta-front mouth bar sands, and sheet sands. Stratigraphically, the Ziniquanzi Formation (E_1-$_2z$) is subdivided into three members (from base to top): $E_{1\text{-}2Z1}$, $E_{1\text{-}2Z2}$, and $E_{1\text{-}2Z3}$. The middle member, $E_{1\text{-}2Z2}$, is the target reservoir interval in this area. Based on the presence of internal mudstone interbeds, $E_{1\text{-}2Z2}$ can be further divided (from top to bottom) into three gas-bearing layers: $E_{1\text{-}2Z2}^{1\text{-}1}$, $E_{1\text{-}2Z2}^{1\text{-}2}$, and $E_{1\text{-}2Z2}^{2}$.

The gas reservoirs of the Ziniquanzi Formation in the Hutubi anticline are anticline traps situated in the downthrown (footwall) block of a major thrust fault (the southern Hutubi Fault). The $E_{1\text{-}2Z2}^{1}$ gas reservoir (comprising layers $E_{1\text{-}2Z2}^{1\text{-}1}$ and $E_{1\text{-}2Z2}^{1\text{-}2}$) is a condensate gas reservoir with edge water. It is a structural-lithologic trap that exhibits a generally layered configuration. This reservoir is bounded by the Hutubi Fault to the south, while its extent in other directions is controlled by the combination of structural framework and lithological variation. Similarly, the $E_{1\text{-}2Z2}^{2}$ gas reservoir is a condensate gas reservoir with bottom water, also governed by both structural and lithological controls. It is bounded to the south by the Hutubi Fault, and in the other directions its limits are defined by the structural setting and lithologic changes.

3 Methodology

3.1 Experiments

In this study, rock samples were collected from the second member of the Ziniquanzi Formation in the Hutubi gas reservoir of the Tarim Basin, at a burial depth of 3,520–3,700 m. All experiments were conducted at the State Key Laboratory of Petroleum Resources and Engineering, China University of Petroleum (Beijing). Prior to analysis, standard cylindrical core plug samples (2.5 cm in diameter) were extracted with a mixture of ethanol and chloroform for approximately 36 h to remove residual oil and salts. The samples were then dried at 120 °C for 24 h in a constant-temperature oven. Porosity and permeability measurements were conducted using a fully automated porosimeter–permeameter (Model AP-608).

Porosity was measured by the helium expansion method and gas permeability by a steady-state method, in accordance with SY/T 5336-2006 (Method for Determining Rock Porosity and Permeability). The measurement error was within ±0.5% for porosity and ±5% for permeability.

Thin sections were prepared by impregnating the samples with epoxy resin, cutting and grinding to a thickness of approximately 30 μm, and staining to distinguish minerals. These thin sections were

then examined under a Zeiss polarizing microscope equipped with a cathodoluminescence apparatus, allowing quantitative analysis of mineral composition and pore structure. The section thickness was controlled within ±2 μm, in accordance with SY/T 5913-2012 (Rock Thin Section Identification Method).

High-pressure mercury intrusion was carried out using an AutoPore IV 9500 mercury porosimeter, in accordance with SY/T 5346-2005 (Method for Determining Rock Capillary Pressure Curves). Dried rock samples (1–2 cm^3 in volume) were subjected to incremental pressures from 0.1 to 200 MPa, and the cumulative mercury intrusion volume at each pressure step was recorded to generate capillary pressure curves. The Washburn equation was applied to correct the data. The intrusion–extrusion hysteresis loop was analyzed to determine parameters such as the median capillary pressure and mercury withdrawal efficiency. These parameters were used to quantitatively characterize pore-throat connectivity and effective flowing porosity.

3.2 3D geological modeling

In this study, three-dimensional geological modeling of the study area was performed using Petrel software, and two high-resolution geological models were constructed for the $E_{1\text{-}2Z3}$ (caprock) and $E_{1\text{-}2Z2}$ (target reservoir) formations. The modeling workflow strictly followed the sequence of geological interpretation, data integration, model construction, and quality control. Specifically, to ensure the accuracy of the geological model and meet the requirements of numerical simulation, the $E_{1\text{-}2Z2}$ reservoir formation was subdivided into finer sub-layers on the basis of its stratigraphic framework by integrating marker beds, stratigraphic cycles, well log characteristics, and reasonable thickness distribution; as a result, a total of 10 sub-layers with 15 layer codes were defined (Table 1). Subsequently, based on the coordinate trajectories of 42 wells, well log interpretations (including the sub-layer division data for the 10 sub-layers), core analyses, and eight structural maps, a three-dimensional model comprising 170 million grid cells was constructed using a 10 m × 10 m horizontal grid with a vertical resolution of 0.5–1.0 m. The modeling process first established a fault model by integrating well and seismic data to define five reverse faults (maximum throw of 130 m). A "structural map + horizon correction" approach (three smoothing iterations with a damping factor of 1,000 m) was applied to construct a detailed structural framework. Next, constrained by the results of sedimentary facies studies, sequential Gaussian simulation was used to perform lithofacies modeling (refined deltaic sand bodies) and property modeling (porosity and permeability). Finally, after validating the model with seismic attribute data and well data calibration (error <5%), a three-dimensional geological model reflecting the heterogeneity of the reservoir at depths between −2,670 and −3,350 m was obtained, providing a centimeter-scale precision geological basis for dynamic analysis of the gas storage reservoir. Notably, a key innovation of this study is the application of an "independent sub-layer gridding" technique to control the morphology of individual sand bodies. Additionally, the spatial variability of formation thickness was quantified through coefficient-of-variation analysis (0.98-2.61). These measures ensure that the geological model adheres to sedimentological principles while capturing abrupt inter-well parameter changes. In the numerical simulations, a criterion based on the gas saturation threshold was introduced: when gas saturation falls below the critical value of 15%, the corresponding region is defined as the "effective water-invaded zone." This threshold was derived from laboratory measurements of irreducible gas saturation and effectively represents the mobility limit of the gas phase within the pore system. In addition, during model validation, anomalous increases in pore pressure were employed as an auxiliary indicator of water invasion, thereby improving the robustness of boundary identification and enhancing the physical interpretability of the results. To validate the model accuracy, the simulation results yielded a geological reserve of 118.19×10^8 m^3, which is consistent with the measured reserve of 119.70×10^8 m^3, with a relative error of only 1.3%.

3.3 Methods for evaluating aquifer energy and water invasion intensity

3.3.1 Static evaluation of aquifer energy

The static evaluation method is primarily based on geological, logging, and core data, aiming to conduct a preliminary assessment of aquifer energy during the early stages of oil and gas field development. This approach does not rely on production dynamic data, making it particularly suitable for undeveloped or early-stage reservoirs. The core of static evaluation lies in estimating the aquifer volume to preliminarily determine the magnitude of the aquifer energy. The volumetric method serves as the most fundamental static evaluation technique, wherein the size of the aquifer is estimated by calculating the geometric volume of the aquifer and incorporating key petrophysical parameters, as shown in Equation 1.

$$W = \pi\left(R_1^{\,2} - R_2^{\,2}\right) \times h \times \varphi \times \left(1 - S_{wi}\right) \tag{1}$$

In this equation, R_1 denotes the outer radius of the aquifer, m; R_2 represents the radius of the gas reservoir, m; h is the effective thickness of the aquifer, m; φ is the average porosity of the aquifer, fraction; S_{wi} is the irreducible water saturation of the aquifer, fraction.

3.3.2 Dynamic evaluation of aquifer energy

In contrast to static methods, dynamic evaluation techniques utilize production dynamic data—such as pressure, gas production rate, and water cut—to quantitatively assess aquifer energy. These methods are more accurate than static approaches and can reflect the actual flow characteristics and energy intensity of the aquifer. Dynamic evaluation is particularly applicable to developed reservoirs and comprises production performance analysis, material balance methods (both linear and nonlinear), and numerical simulation techniques.

3.3.2.1 Production performance analysis

The production performance analysis method establishes the relationship between reservoir pressure parameters and cumulative gas production to analyze the dynamic characteristics of the reservoir and the strength of the aquifer energy. This approach

TABLE 1 Subdivision of sublayers in the second member of the Paleogene Ziniquanzi Formation.

Member	$E_{1\text{-}2z2}^{1\text{-}1}$			$E_{1\text{-}2z2}^{1\text{-}2}$								$E_{1\text{-}2z2}^{2}$			
Sub-layer	$z_2^{1\text{-}1\text{-}1}$	$z_2^{1\text{-}1\text{-}2}$	$z_2^{1\text{-}1\text{-}3}$	$z_2^{1\text{-}2\text{-}1}$		$z_2^{1\text{-}2\text{-}2}$		$z_2^{1\text{-}2\text{-}3}$		$z_2^{1\text{-}2\text{-}4}$		$z_2^{2\text{-}1}$		$z_2^{2\text{-}2}$	$z_2^{2\text{-}3}$
Layer code	1	2	3	4	5	6	7	8	9	10	11	12	13	14	15

offers the advantages of early warning capability and minimal data requirements; however, attention must be paid to the quality of pressure data and the accuracy of PVT parameters. Future developments may focus on intelligent analysis and high-precision interpretation to further support reservoir management decisions (Xu et al., 2021).

1. For volumetric gas reservoirs without aquifer support, the pressure-production relationship can be expressed as shown in Equation 2.

$$P/Z = (P_i/Z_i)\left(1 - G_p/G\right) \tag{2}$$

In this equation, P/Z is the apparent formation pressure (MPa), defined as the ratio of the measured pressure to the gas deviation factor; G_p is the cumulative gas production, 10^8 m^3; G is the geological reserves, 10^8 m^3.

2. When considering the elastic expansion of the rock matrix and irreducible water in closed reservoirs, a corrected pressure parameter is adopted, as indicated in Equations 3, 4.

$$P_F = (P/Z)/(1 - C_c \times \Delta P) \tag{3}$$

$$C_c = \left(C_p + S_{wi} \times C_w\right)/(1 - S_{wi}) \tag{4}$$

In this equation, P_F is the pressure of the closed gas reservoir, MPa; Cc is the total compressibility coefficient, MPa^{-1}; C_p is the rock compressibility coefficient, MPa^{-1}; C_W is the water compressibility coefficient, MPa^{-1}; and S_{wi} is the irreducible water saturation, dimensionless.

3. For water-driven gas reservoirs with active aquifer encroachment, a storage volume coefficient is introduced, as shown in Equations 5, 6.

$$P_H = (P/Z)/(1 - C_c \times \Delta P - \omega) \tag{5}$$

$$\omega = W/\left(G \times B_{gi}\right) \tag{6}$$

In this equation, P_H is the pressure of the water-drive gas reservoir, MPa; ω is the water storage volume coefficient, dimensionless; W is the water influx, m^3; B_{gi} is the initial gas formation volume factor, dimensionless.

By analyzing the linear correlation (R^2) and curve morphology between pressure and cumulative production, the reservoir type and aquifer energy intensity can be diagnosed. A higher R^2 value ($R^2 > 0.95$) indicates weak aquifer support, whereas a significant upward curvature ($R^2 < 0.8$) suggests strong water drive characteristics.

Furthermore, the difference between P_F–G_P and P_H–G_P curves can be used to calculate the cumulative water influx, as shown in Equation 7.

$$W_e = W_p \times B_p + G \times B_{gi} \times \Delta P_F \times Z/P \tag{7}$$

In this equation, W_e is the cumulative water influx, m^3; W_p is the cumulative water production, m^3; B_p is the water formation volume factor, dimensionless.

3.3.2.2 Material balance method

The material balance method is a core approach in gas reservoir engineering for evaluating dynamic behavior and water invasion characteristics. Its basic principle relies on the law of mass conservation. By establishing the relationship between fluid production and pressure changes during reservoir development, this method infers reservoir parameters and the energy of the aquifer (water drive). For a water-drive normal-pressure gas reservoir, the material balance equation can be expressed (as shown in Equation 8) (Patacchini, 2017).

$$G_p \times B_g + W_p \times B_w = G \times \left(B_g - B_{gi}\right) + W_e + GB_{gi} \left\{\left(C_w \times S_{wi} + C_p\right)/(1 - S_{wi})\right\} \Delta P \tag{8}$$

Equation 8 can be rearranged and simplified into the form shown in Equation 9:

$$\left(G_p \times B_g + W_p \times B_w\right)/\left(G \times B_{gi}\right) = B_g/B_{gi} - 1 + W_e/\left(G \times B_{gi}\right) + C_e \times \Delta P \tag{9}$$

In this equation, G_p represents the cumulative gas production10^8 m^3; B_g denotes the gas formation volume factor at the current pressure, dimensionless; C_e is the effective compressibility calculated as $(C_wS_{wi} + C_p)/(1\text{-}S_{wi})$.

Equations 10, 11 relate the formation volume factors Bg and Bgi at different conditions.

$$B_g = (ZTP_0)/(T_0P) \tag{10}$$

$$B_{gi} = (Z_iTP_0)/(T_0P_i) \tag{11}$$

In this equation, T_0 represents the standard surface temperature, K; T is the average reservoir temperature, K; P_0 is the standard surface pressure, MPa; P_i is the initial reservoir pressure, MPa; Z_i is the initial gas deviation factor, dimensionless; Zis the gas deviation factor at pressure P, dimensionless.

Substituting Equations 10, 11 into Equation 9 and rearranging yields Equation 12.

$$\left(1 - G_p/G\right) \times (P_i/Z_i)/(P/Z) = -W_e/\left(G \times B_{gi}\right) - C_e \times \Delta P + \left\{\left(W_p \times B_w\right)/\left(G \times B_{gi}\right)\right\} + 1 \tag{12}$$

The water invasion volume can be expressed as shown in Equation 13.

$$W_e = V_{pw} \times \left(C_w + C_p\right)\Delta P \tag{13}$$

We also define the water multiplicity n by Equation 14.

$$n = V_{pw}/\left\{\left(G \times B_{gi}\right)/\left(1 - S_{wi}\right)\right\} \tag{14}$$

In this equation, V_{pw}denotes the aquifer pore volume, m^3; nrepresents the aquifer multiple, reflecting the strength of the aquifer drive, dimensionless.

Substituting Equations 13, 14 into Equation 12 gives the form of Equation 15, which relates the production and pressure data with n and other parameters.

$$\left(1 - G_p/G\right) \times \left(P_i/Z_i\right)/\left(P/Z\right) = -\left\{n \times \left(C_w + C_f\right)/\left(1 - S_{wi}\right)\right\} \times \Delta P + \left\{\left(W_p \times B_w\right)/\left(G \times B_{gi}\right)\right\} + 1 \tag{15}$$

From Equation 15, one can plot the term $(1-G_p/G)\cdot(P_i/Z_i)/(P/Z)$ versus ΔP. The slope of this plot yields the water multiplicity n, and the intercept corresponds to the initial water invasion volume. This graphical method thus allows determination of the aquifer energy and initial water invasion based on production and pressure history.

3.3.2.3 Nonlinear material balance method

The nonlinear material balance method is an important approach in the dynamic analysis of water-drive gas reservoirs. By introducing dimensionless parameters to establish the relationship between pressure and recovery factor, it effectively evaluates the strength of the aquifer energy. For water-drive gas reservoirs under normal pressure conditions, rock compressibility and bound-water expansion can be neglected. Accordingly, the material balance principle for a water-drive gas reservoir can be simplified as shown in Equation 16.

$$1 = \left(P_i/Z_i\right)/\left(P/Z\right) \times \left(1 - G_p/G\right) + \left\{\left(W_e - W_p \times B_w\right)/\left(G \times B_{gi}\right)\right\} \tag{16}$$

In this context, the key dimensionless parameters are defined as follows:

$$\varphi_D = \left(P/Z\right)/\left(P_i/Z_i\right) \tag{17}$$

$$R = G_p/G \tag{18}$$

$$\omega = \left(W_e - W_p \times B_w\right)/\left(G \times B_{\mathrm{gi}}\right) \tag{19}$$

$$B = Ln\omega/Ln \tag{20}$$

In this equation, φ_D represents the dimensionless pseudo-pressure; R denotes the recovery factor (as a fraction); ω is the dimensionless gas volumetric coefficient of the aquifer, and B is the dimensionless parameter reflecting the strength of the aquifer energy.

By substituting Equations 17–20 into Equation 16, the following relationship can be obtained the following relationship can be obtained (see Equation 21):

$$\varphi_D = \left(1 - R\right)/\left(1 - R^B\right) \tag{21}$$

This equation establishes the theoretical relationship between dimensionless pressure and recovery factor. The morphology of the φ_D-R curve directly reflects the characteristics of the aquifer energy: 1) When B→ ∞, the curve degenerates into a straight line with a slope of −1, characteristic of a constant-volume gas reservoir; 2) When B = 1, the curve is a horizontal line, representing a rigid water drive system; 3) When 1 < B < ∞, the curve exhibits a nonlinear shape, and the smaller the value of B, the stronger the aquifer energy.

Based on the determined dynamic gas reserves and water influx characteristics, the cumulative water influx at different production times can be calculated by Equation 22.

$$W_e = \left(G_p/G\right)^B \times G \times B_{gi} + W_p B_w \tag{22}$$

3.3.2.4 Numerical simulation method

The numerical simulation approach involves constructing a three-dimensional model of the reservoir–aquifer system. Unstructured grids are employed to locally refine the aquifer region. Constant-pressure boundaries simulate an infinite aquifer, whereas closed boundaries represent a finite aquifer. Key parameters such as the gas–water contact depth, aquifer porosity, and permeability are initialized. For fractured reservoirs, a dual-porosity model is required. A multi-stage history-matching optimization is then applied: reservoir pressure is matched first (error <5%) by adjusting the aquifer volume and permeability, and water saturation is matched next (error <10%) by modifying the relative permeability curves. Finally, the aquifer multiplier n is determined (n < 5 indicates a limited aquifer, 5 ≤ n ≤ 20 a moderate aquifer, and n > 20 a strong aquifer), achieving a simultaneous match of pressure, production, and water saturation. By integrating four-dimensional seismic data and inter-well tracer monitoring, the advancement rate and direction of the water invasion front can be predicted accurately. Conservative, baseline, and optimistic scenarios are then used to forecast pressure changes over the next 5–10 years, enabling optimization of drainage well placement. The numerical simulation method includes constructing a three-dimensional numerical model of the reservoir–aquifer system. An unstructured grid is used to locally refine the aquifer region, and boundary conditions are set to simulate either an infinite aquifer (constant-pressure boundary) or a finite aquifer (closed boundary). Key parameters such as the gas–water contact depth, aquifer porosity, and permeability are initialized. For reservoirs with significant fracturing, a dual-porosity model must be implemented. A multi-stage history-matching optimization process is then employed: reservoir pressure is first matched (error <5%) by adjusting the aquifer volume and permeability.

3.3.3 Water invasion intensity evaluation method

Previous studies have evaluated water invasion intensity in gas reservoirs using the Water Drive Index (DI). This index is derived from actual gas production, water injection, and reservoir pressure data collected during the water-drive process and provides a quantitative measure of water invasion (Feng et al., 2015). The DI represents the fraction of driving energy contributed by aquifer support (edge or bottom water) relative to the total driving energy, as shown in Equation 23.

$$DI_e = W_e/\left(G_p B_g + W_p B_w\right) \tag{23}$$

Accordingly, elastic water-drive gas reservoirs are classified based on the DI value as follows: strong water drive (DI > 0.3),

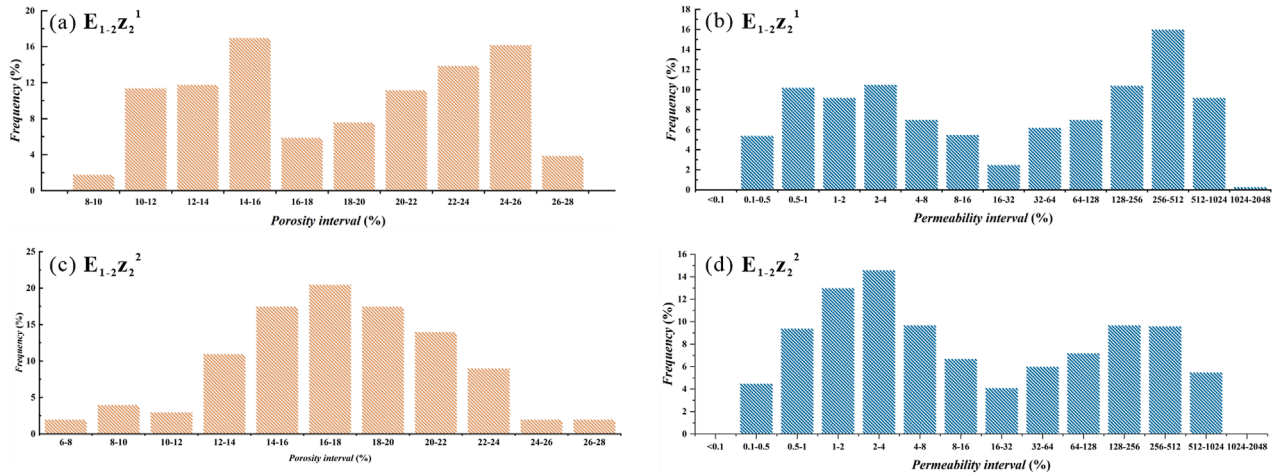

FIGURE 2
Petrophysical properties for the second member of the Paleogene Ziniquanzi Formation sandstone from the Hutubi gas storage: **(a)** The porosity of the $E_{1-2}Z_2^1$ gas layer; **(b)** The permeability of the $E_{1-2}Z_2^1$ gas layer; **(c)** The porosity of the $E_{1-2}Z_2^2$ gas layer; **(d)** The permeability of the $E_{1-2}Z_2^2$ gas layer.

moderate water drive ($0.1 \leq DI \leq 0.3$), and weak water drive ($DI < 0.1$).

4 Result

4.1 Microscopic characteristics of the UGS reservoir

4.1.1 Petrophysical properties

The petrophysical characteristics of the E_{1-2Z2}^1 and E_{1-2Z2}^2 gas layers of the Ziniquanzi Formation exhibit notable differences, specifically reflected in similar porosity but significant variation in permeability (Figure 2). The porosity of the E_{1-2Z2}^1 gas layer ranges from 9.0% to 26.0%, with an average of 16.4%, and its permeability ranges from 0.2 to 1,300 mD, averaging 39.3 mD. In comparison, the porosity of the E_{1-2Z2}^2 gas layer ranges from 9.5% to 25.2%, with an average of 18.1%, while the permeability varies from 0.56 to 604 mD, with an average of 31.7 mD. According to the classification standards for continental clastic reservoir rocks in China, the Ziniquanzi Formation (Second Member) reservoir of the Hutubi Gas Field is categorized as a medium-porosity and permeability reservoir.

4.1.2 Lithological and mineralogical characteristics

Thin-section analysis reveals pronounced regional contrasts in reservoir characteristics. In the central zone, the reservoir is dominated by fine sandstone with relatively good sorting. Pores are mainly intergranular, accompanied by minor dissolution pores and microfractures, resulting in overall higher porosity and connectivity (Figure 3a). In contrast, the western zone is primarily composed of coarse siltstone with moderate sorting, where pore space consists of both intergranular pores and clay-related intercrystalline pores, yielding lower porosity and connectivity (Figure 3b). The eastern zone is dominated by fine siltstone with poor sorting and pervasive basal cementation; pores are mainly intergranular and intercrystalline, but overall porosity and connectivity are the lowest (Figure 3c). Overall, pore structure is most favorable in the central zone, intermediate in the west, and poorest in the east, underscoring distinct spatial heterogeneity across the reservoir.

The lithology of the Second Member is dominated by fine-grained sandstone and siltstone. The mineral composition is primarily quartz (ranging from 38.00% to 59.67%, with an average of 48.00%), followed by feldspar (21.50%–30.60%, averaging 28.00%) and volcanic rock fragments (3.57%–18.14%, averaging 15.00%). The pore-filling materials mainly consist of ferruginous clay and sericitized clay, while calcite is the dominant cementing mineral. Based on the ratio of stable minerals (quartz) to unstable minerals (feldspar plus lithic fragments), the compositional maturity of the Second Member reservoir ranges from 0.61 to 1.48, indicating a moderate to high compositional maturity (Table 2).

4.1.3 Pore structure characteristics

High-pressure mercury intrusion (HPMI) results for samples from the Second Member of the Ziniquanzi Formation exhibit significant regional variations:

1. Samples from the central part of the study area (HUK18-3,556.4 m, KUKJ3-3,058.67 m) show pore structures characterized by high mercury intrusion saturation (92.19%–88.55%), low displacement pressures (0.09–0.11 MPa), and a pronounced "plateau segment" in the mercury intrusion curves. The lower limit of the main flow pore radius is relatively large (1.28–3.013 μm), indicating high pore utilization efficiency, good pore connectivity, a concentrated pore size distribution (dominant peak radius at 2.147 μm), and strong effective flow capacity (Figure 4a).
2. Samples from the western (HUK3) and eastern (HU001) parts of the study area exhibit pore structures characterized by low mercury intrusion saturation (51.44%–50.74%), high displacement pressures (0.78–4.39 MPa), and steep mercury intrusion curves. The lower limit of the main flow pore radius is relatively small (0.028–0.076 μm), suggesting

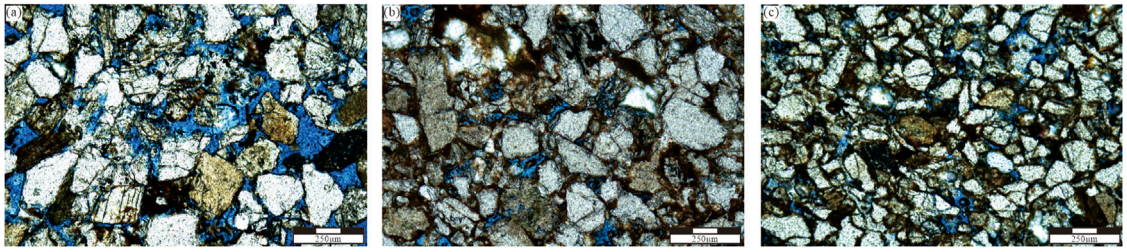

FIGURE 3
Pore space observed from thin sections for the second member of the Paleogene Ziniquanzi Formation sandstone from the Hutubi gas storage: **(a)** the central zone; **(b)** the western zone; **(c)** the eastern zone..

low pore utilization efficiency, poor pore connectivity, relatively uniform pore size distribution, and weak effective flow capacity (Figure 4b).

4.2 Macroscopic distribution characteristics of the UGS reservoir

4.2.1 Distribution characteristics of reservoir sand bodies and interlayers

Sand bodies of the second member of the Ziniquanzi Formation in the Hutubi gas reservoir are continuously distributed and well connected. The $E_{1\text{-}2Z2}^{1-1}$ sand body is relatively underdeveloped, with a thickness of 5.0–17.0 m, and is thickest in the west and thinnest in the east (Figure 5a). The $E_{1\text{-}2Z2}^{1-2}$ sand body has a thickness of 15.0–33.0 m and is distributed in a southwest-northeast elongated strip, mainly in the eastern and central parts of the study area, thinning toward the west and south (Figure 5b). The $E_{1\text{-}2Z2}^{2}$ sand body is relatively well developed, with a thickness of 25.0–30.0 m, and is primarily distributed in the east and central regions (Figure 5c).

The gas layers of the Ziniquanzi Formation are thick and contain stable mudstone interlayers between sublayers. Stable mudstone interlayers occur between the $E_{1\text{-}2Z2}^{1}$ and $E_{1\text{-}2Z2}^{2}$ layers, and between the $E_{1\text{-}2Z2}^{1-1}$ and $E_{1\text{-}2Z2}^{1-2}$ sublayers. Between $E_{1\text{-}2Z2}^{1}$ and $E_{1\text{-}2Z2}^{2}$, the interlayer thickness decreases toward the west (it is thicker in the east) (Figure 5d). Between $E_{1\text{-}2Z2}^{1-1}$ and $E_{1\text{-}2Z2}^{1-2}$, the interlayer thickens westward (Figure 5e). In the $E_{1\text{-}2Z2}^{1}$ layer, gas layers and interlayers alternate over 15 layers, mainly composed of mudstone and argillaceous siltstone, with individual layer thicknesses ranging from 13.0 to 36.3 m. In contrast, the $E_{1\text{-}2Z2}^{2}$ layer contains only three interlayers, primarily argillaceous siltstone, with thicknesses between 0.6 and 10.3 m.

4.2.2 Istribution characteristics of reservoir physical properties

Based on core analyses, core data were used to calibrate logging curves and establish mathematical models relating logging data to porosity and permeability, enabling mapping of these properties across the study area. The porosity distribution in the second member of the Ziniquanzi Formation is stable; high-porosity zones form northeast–southwest–trending elongate strips with good connectivity. The average porosity in the western region (13.0%) is slightly lower than in the central and eastern regions. The average porosity of the $E_{1\text{-}2Z2}^{1-1}$, $E_{1\text{-}2Z2}^{1-2}$, and $E_{1\text{-}2Z2}^{2}$ layers increases gradually from top to bottom (Figures 6a–c). Overall, the reservoir exhibits good permeability, with most areas having permeability values greater than 25.0 mD. In plan view, the reservoir shows strong heterogeneity. High-permeability zones occur in northeast-southwest strips, with significant variations by layer: in the $E_{1\text{-}2Z2}^{1-1}$ layer, these zones are mainly in the western and central parts (Figure 6d); in the $E_{1\text{-}2Z2}^{1-2}$ layer, they are in the central part (Figure 6e); and in the $E_{1\text{-}2Z2}^{2}$ layer, they are distributed in the central and eastern parts (Figure 6f). All these high-permeability zones have permeability values exceeding 60 mD. The formation coefficient reflects the productivity of injection and production wells in the gas storage reservoir; larger values indicate higher productivity. For the effective reservoirs in the $E_{1\text{-}2Z2}^{1-1}$, $E_{1\text{-}2Z2}^{1-2}$, and $E_{1\text{-}2Z2}^{2}$ layers, the formation coefficients range from 1 to 571.0 mD·m (mean 66.0 mD·m), 3.7 to 2,659.0 mD·m (mean 370.0 mD·m), and 8.0 to 3,914.2 mD·m (mean 521.0 mD·m), respectively, indicating an increasing trend from top to bottom (Figures 6g–i). High values of the formation coefficient are distributed in strip-like zones. In the $E_{1\text{-}2Z2}^{1-1}$ layer, formation coefficients form blocky high-value zones along the east-west direction, with good connectivity along the north-south direction, consistent with sedimentary trends. The $E_{1\text{-}2Z2}^{1-2}$ layer shows blocky high values in uplifted areas with good lateral connectivity, whereas the western region has lower values. The $E_{1\text{-}2Z2}^{2}$ layer exhibits a north-south zonation in formation coefficients (Figure 6c).

4.2.3 Reservoir heterogeneity characteristics

4.2.3.1 Intra-layer heterogeneity

The permeability of sand bodies in the second member of the Ziniquanzi Formation ranges from 0.18 to 845.0 mD. The permeability variation coefficients are all greater than 1.3, advance coefficients exceed 4.6, and contrast values exceed 1,000, indicating strong intra-layer heterogeneity (Table 3). Despite significant permeability fluctuations, the vertical-to-horizontal permeability ratio remains between 0.69 and 0.83 (Table 3), indicating relatively uniform vertical permeability. This suggests that injected or produced gas can be evenly distributed over a considerable thickness.

TABLE 2 Mineral composition of the second member for the Paleogene Ziniquanzi Formation sandstone from the Hutubi gas storage.

Well	Formation	Main rock components/%					Fillings/%				Quartz/(Feldspar + Debris)
		Quartz	Feldspar	Tuff	Mica	Others	Heterobase			Cement	
							Iron mud	Hydromica mud	Others	Calcite	
HU2	$E_{1\text{-}2Z1}^{2}$	40.75	26.25	13.75	0.25	12.5	4.25			2.67	0.69
	$E_{1\text{-}2Z2}^{1}$	38.00	30.00	15.00	2.00	8.00				4.00	0.61
HU001	$E_{1\text{-}2Z2}^{1}$	53.11	30.60		0.40	15.1	5.80		2.60	7.30	1.13
	$E_{1\text{-}2Z3}^{1}$	51.41	21.82	17.26		3.17	2.76		2.10		1.05
HU002	$E_{1\text{-}2Z2}^{1}$	59.67	21.50	5.33	1.00	8.47	1.50	4.83		3.00	1.47
	$E_{1\text{-}2Z2}^{2}$	54.43	28.14	3.57	0.67	11.72		8.14		2.14	1.19
	$E_{1\text{-}2Z3}^{1}$	53.28	23.90	11.31	0.28	6.60	0.03	7.51		2.59	1.14
HU2002	$E_{1\text{-}2Z2}^{1}$	47.83	27.68	13.92	2.65	7.38	3.51	0.46	0.90	2.17	0.92
	$E_{1\text{-}2Z2}^{2}$	47.76	28.89	16.29	0.95	6.02	4.32		1.95	1.87	0.91
	$E_{1\text{-}2Z3}^{1}$	48.07	28.21	18.14	0.21	5.21	3.93		2.36	3.64	0.92
Total	$E_{1\text{-}2Z2}^{1}$	49.65	27.45	11.42	1.51	9.74	3.60	2.65	1.75	4.12	1.03
	$E_{1\text{-}2Z2}^{2}$	51.10	28.52	9.93	0.81	8.87	4.32	8.14	1.95	2.01	1.05
	$E_{1\text{-}2Z2}$	50.13	27.80	10.82	1.28	9.45	3.78	4.48	1.82	3.41	1.04
	Average	48.00	28.00	15.00	0.80	8.20	2.60	2.30	1.00	2.90	0.92

10.3389/feart.2025.1650076

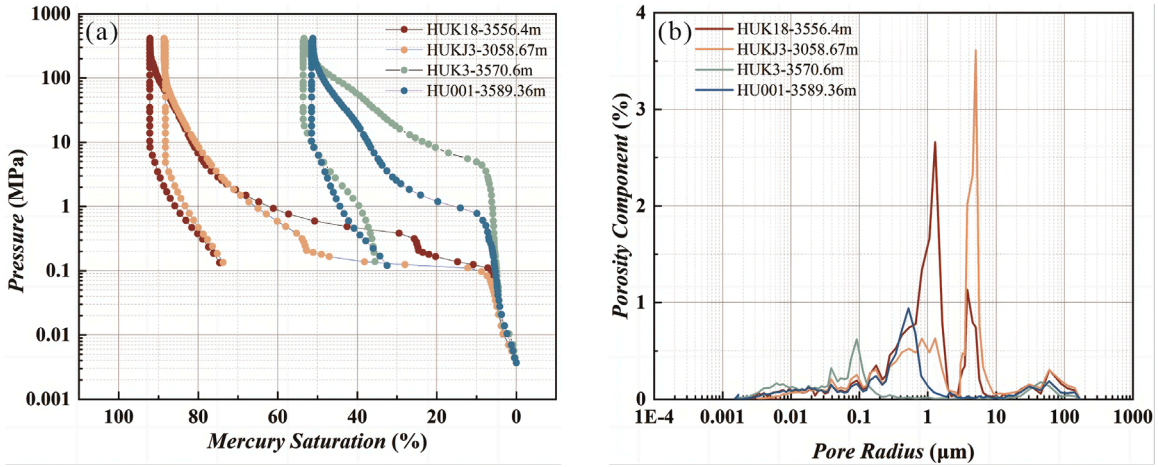

FIGURE 4
Pore structure characterization using a high-pressure mercury intrusion experiment for the second member of the Paleogene Ziniquanzi Formation sandstone from the Hutubi gas storage: **(a)** capillary pressure curve; **(b)** pore size distribution curve.

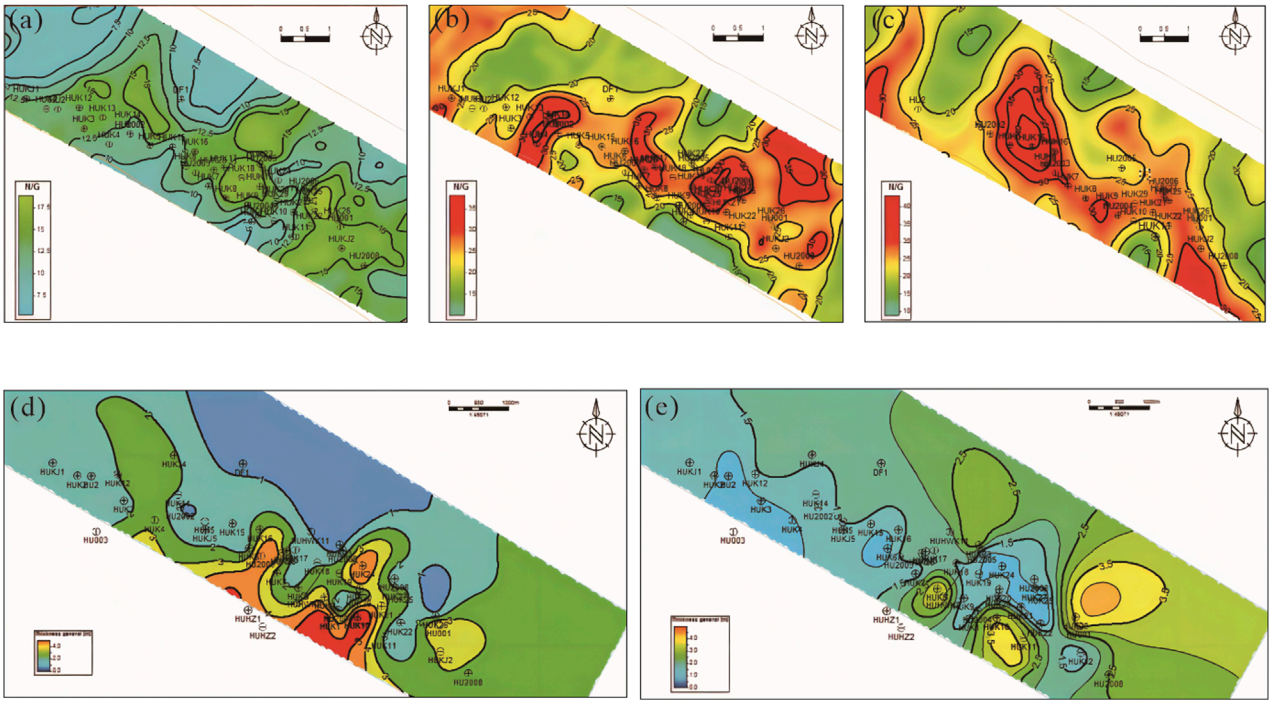

FIGURE 5
Distribution Characteristics of sandstone bodies and interlayer for the second member of the Paleogene Ziniquanzi Formation sandstone from the Hutubi gas storage: **(a–c)** The sandstone bodies distribution characteristics of E1-2z21-1, E1-2z21-2 and E1-2z22; **(d,e)** The interlayer distribution characteristics between E1-2z21 and E1-2z22, E1-2z21-1 and E1-2z21-2.

4.2.3.2 Inter-layer heterogeneity

Inter-layer heterogeneity among the main gas-bearing layers ($E_{1\text{-}2Z2}^{1-1}$, $E_{1\text{-}2Z2}^{1-2}$, $E_{1\text{-}2Z2}^{2}$) is also strong. Permeability variation coefficients range from 1.334 to 1.394, advance coefficients from 4.09 to 5.92, and contrast values from 4674.07 to 8,030.78 (Table 4). The average single-sand-body thicknesses are 2.0 m, 2.6 m, and 7.1 m for $E_{1\text{-}2Z2}^{1-1}$, $E_{1\text{-}2Z2}^{1-2}$, and $E_{1\text{-}2Z2}^{2}$, respectively; effective thickness coefficients range from 0.61 to 0.75, and sandstone densities from 0.61 to 0.77. The $E_{1\text{-}2Z2}^{1-1}$ layer has significantly higher layering coefficients and interlayer frequency than the $E_{1\text{-}2Z2}^{1-2}$ and $E_{1\text{-}2Z2}^{2}$ layers, indicating the strongest heterogeneity in $E_{1\text{-}2Z2}^{1-1}$. Overall, inter-layer heterogeneity decreases from the top to the bottom layers.

4.2.3.3 Planar heterogeneity

Planar heterogeneity in the Ziniquanzi Formation is primarily caused by variations in sand body geometry, porosity, and permeability. All effective reservoirs in the $E_{1\text{-}2Z2}^{1-1}$, $E_{1\text{-}2Z2}^{1-2}$,

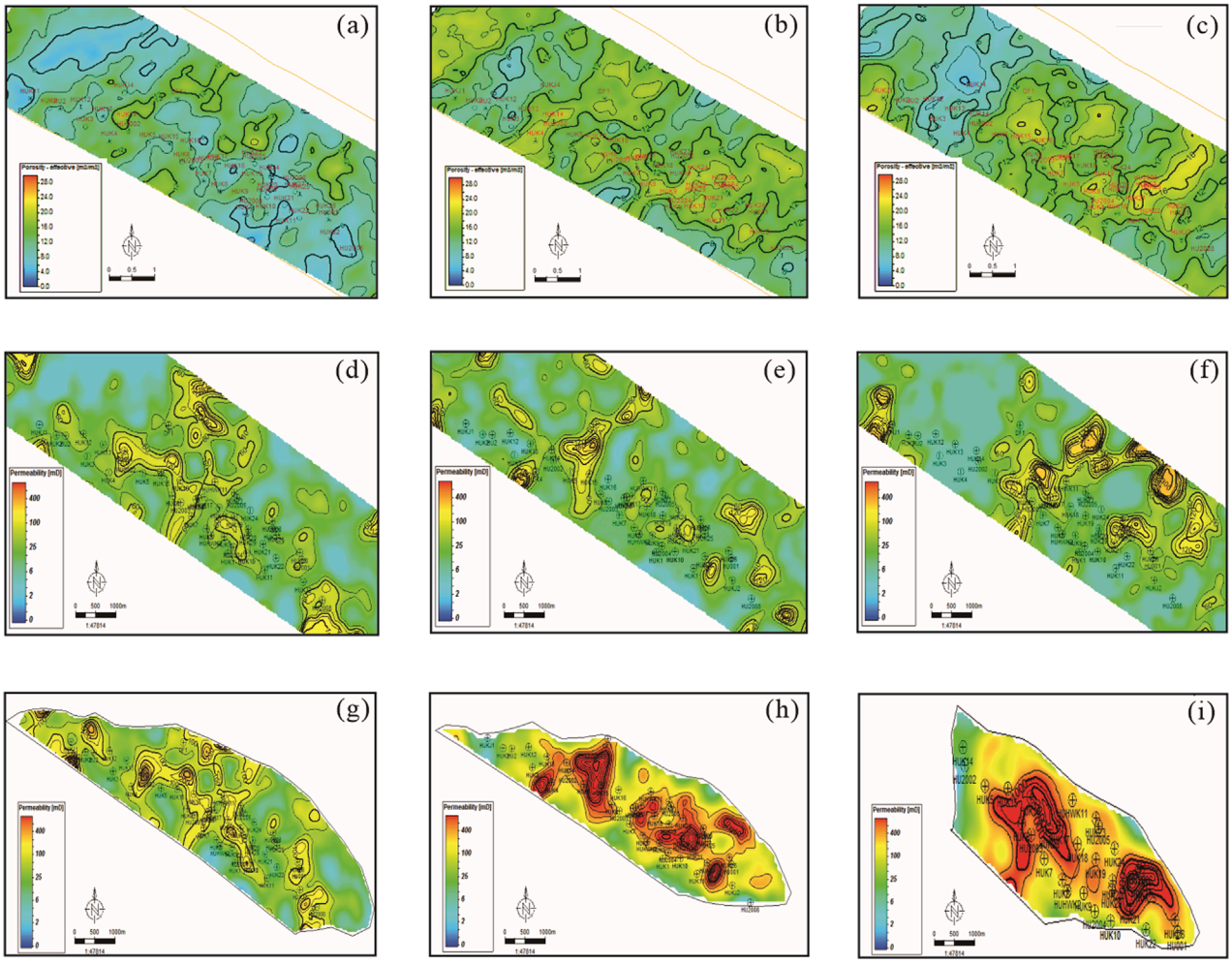

FIGURE 6
The Distribution Characteristics of porosity, permeability and formation factor of the second member of the Paleogene Ziniquanzi Formation sandstone from the Hutubi gas storage: **(a–c)** The porosity distribution characteristics of E1-2z21-1, E1-2z21-2 and E1-2z22; **(d–f)** The permeability distribution characteristics of E1-2z21-1, E1-2z21-2 and E1-2z22; **(g–i)** The formation factor distribution characteristics of E1-2z21-1, E1-2z21-2 and E1-2z22.

and $E_{1\text{-}2Z2}^{2}$ layers have formation coefficients exceeding 0.75. Sand bodies are extensively distributed with stable thicknesses between wells. However, significant planar variations in reservoir physical properties are observed: high-quality regions form northeast–southwest strips, reflecting strong lateral heterogeneity.

5 Discussion

5.1 Reservoir aquifer energy evaluation

Using multiple static and dynamic methods to comprehensively evaluate the aquifer energy of the Hutubi USG, this study systematically reveals the characteristics of the aquifer energy and its influence mechanism on water invasion. The results indicate that the aquifer energy in the study area is limited and inactive, corresponding to a weak water-drive reservoir:

1. Static geological analysis: Monitoring data of the gas-water contact indicate that after USG construction, the gas-water contact in the western area rose by 8.6 m (to −3,038.4 m) and in the eastern area by 2.3 m, forming a water-invasion transition zone of 4.82 km^2. Using the volumetric method, the volume affected by water invasion was calculated to be 7.93×10^8 m^3.
2. Production indicator curve method: As of October 2012, after more than a decade of production in the Hutubi gas field, the pressure drawdown curve exhibits a clear two-stage evolution (Figure 7a). In the early production period, the P_F-G_p and P_H-G_p curves almost coincided, reflecting the characteristics of a closed constant-volume gas reservoir. From 1999 to 2005, the data points of P_F-G_p deviated from the overall P_H-G_p pressure drawdown curve, indicating limited aquifer energy support; after Well Hu2 was shut in 2006, the pressure drawdown curves coincided, and the gas reservoir reverted to constant-volume behavior, confirming the interruption of aquifer replenishment and a shift in the main drive energy

TABLE 3 Intraformational heterogeneity parameters based on core data.

Formation		Permeability/mD			Variation coefficient	Advance coefficient	Contrast values	Vertical permeability/horizontal permeability		Sample number
		Maximum value	Minimum value	Mean value				Range	Mean value	
E_{1-2Z2}^{1}	E_{1-2Z2}^{1-1}	817.00	0.30	176.45	1.48	4.63	2687.50	0.126 ~ 5.363	0.701	43
	E_{1-2Z2}^{1-2}	845.00	0.48	150.84	1.30	5.60	1760.42	0.006 ~ 2.623	0.69	106
E_{1-2Z2}^{2}		834.00	0.18	76.08	2.41	11.08	7222.22	0.008 ~ 4.471	0.827	179

TABLE 4 Interlayer heterogeneity parameters based on logging data.

Formation		Maximum permeability value/mD	Minimum permeability value/mD	Average permeability/mD	Permeability variation coefficient	Advance coefficient	Contrast value	Well number
E_{1-2Z2}^{1}	E_{1-2Z2}^{1-1}	998.55	0.18	54.67	1.39	5.35	5547.48	42
	E_{1-2Z2}^{1-2}	1201.24	0.03	157.55	1.47	5.92	4674.07	41
E_{1-2Z2}^{2}		1044.00	0.13	126.66	1.33	4.09	8030.78	27

10.3389/feart.2025.1650076

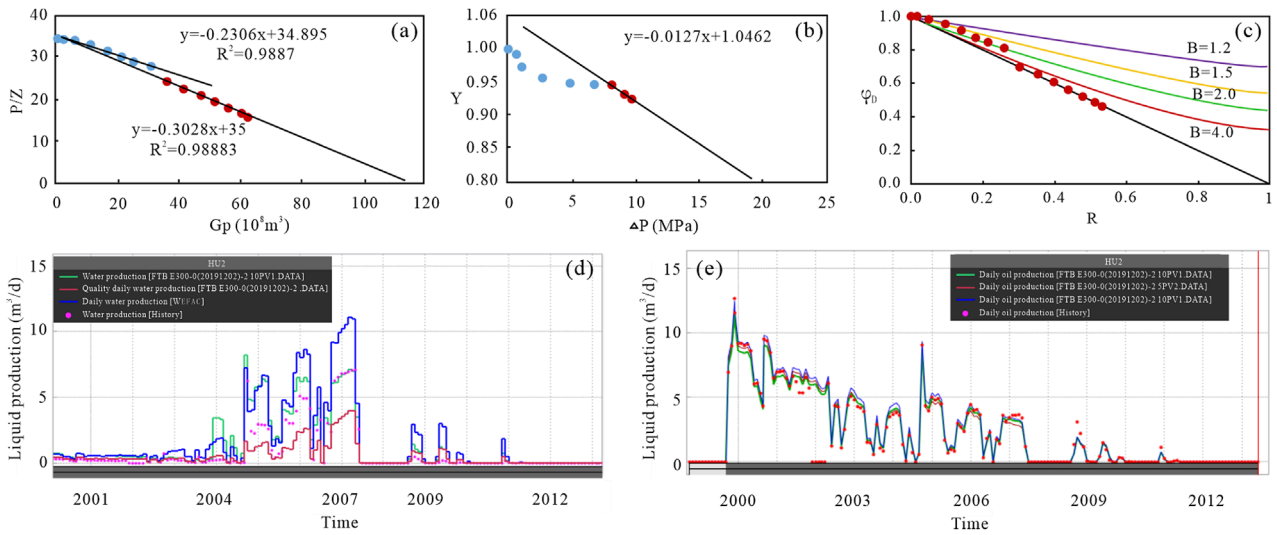

FIGURE 7
Water energy evaluation: **(a)** P/Z-Gp relationship curve of Tubi gas field; **(b)** Material Balance Equation of WaterFlooding Gas Reservoi; **(c)** ψD and R characteristic chart of Tubi gas field; **(d)** Simulation results of daily water production in Huhu 2 well; **(e)** Simulation results of daily oil production in Hu 2 well.

to *in-situ* condensate gas expansion. In summary, the aquifer energy of the Second Member of the Ziniquanzi Formation in the Hutubi gas field is limited and inactive, with minor aquifer energy supplementation during reservoir development.

3. Material balance method: The aquifer energy of the Hutubi USG shows clear staged variations. During pressure decline, the slope of the curve is −0.0126, the aquifer multiple is 5.42, and the cumulative water influx is 63.64 × 10^4 m^3, indicating limited aquifer support (Figure 7b). Further analysis using nonlinear material balance shows that the reservoir development can be divided into two characteristic stages (Figure 7c). In 2000-2005, the parameter B is 1.85, consistent with elastic waterdrive characteristics, reflecting a certain level of aquifer energy support; after 2006, B approaches infinity, indicating the reservoir development shifted to constant-volume depletion and aquifer energy support essentially ceased, with a calculated cumulative water influx of 77.06 × 10^4 m^3.
4. Numerical simulation validation: A locally refined numerical model was established, focusing on Well Hu2 for history matching analysis. The simulation results show that when the aquifer multiple is set to 5, the daily water production fitting error is less than 8% (Figure 7d), and the daily oil production fitting error is controlled within 5% (Figure 7e), achieving optimal history matching. The cumulative water invasion determined by the numerical simulation is 50.2 × 10^4 m^3, with the affected pore volume reaching 356.0 × 10^4 m^3, accounting for 7.9% of the subsurface gas-bearing pore volume (0.45 × 10^8 m^3). Notably, the simulation results are in good agreement with the production indicator curve method and material balance method. All indicators confirm the limited and inactive aquifer energy. In addition, the reservoir water-drive index is 0.025, reflecting a weak water-drive reservoir.

5.2 Water invasion characteristics of the USG reservoir

5.2.1 Gas production stage water invasion characteristics

Prior to the construction of the USG, seven wells were put into production, of which only two wells (Well Hu2 and Well HU 2006) produced formation water, and the produced water volume was limited. Well Hu2 had a cumulative water production of 0.53 × 10^4 m^3 and a maximum water-gas ratio of 0.9 m^3/10^4 m^3. After 2 years of water production, the bottom water-producing interval of the $E_{1\text{-}2Z2}^{1\text{-}2}$ formation was plugged; Well HU2006 encountered water and was quickly flooded, producing a cumulative 0.66 × 10^4 m^3 of water with a water-gas ratio of 2.46 m^3/10^4 m^3 before shut-in. After Well Hu2 began producing water, gas production from the western structural low of the $E_{1\text{-}2Z2}^{1}$ reservoir decreased significantly, exhibiting clear water-invasion characteristics (Figure 8a). Material balance calculations indicate a unit pressure-drop water invasion volume of 6.7 × 10^4 m^3 (Figure 8b), with an estimated connected aquifer volume of 9,054 × 10^4 m^3. Although Well HU2006 in the $E^{1\text{-}2}z_2^{2}$ formation was quickly flooded after encountering water, the pressure decline curve did not show an upward kink (Figure 8c), indicating that only a local bottom-water cone developed and it did not affect the entire reservoir.

Three-dimensional numerical simulation reveals significant selective layer and directional characteristics of reservoir water invasion. In the $E_{1\text{-}2Z2}^{1}$ reservoir, water invasion mainly occurred in the lower main layers 7-11 (from small layer $E_{1\text{-}2Z2}^{1\text{-}2\text{-}2}$ to $E_{1\text{-}2Z2}^{1\text{-}2\text{-}4}$), showing regional differences (taking small layer 7 as an example, Figures 9a,b). In the western zone, the distance from the gas-water contact to Well HU2002 decreased from 1,652.0 m originally to 674.0 m by the end of the production stage, with the

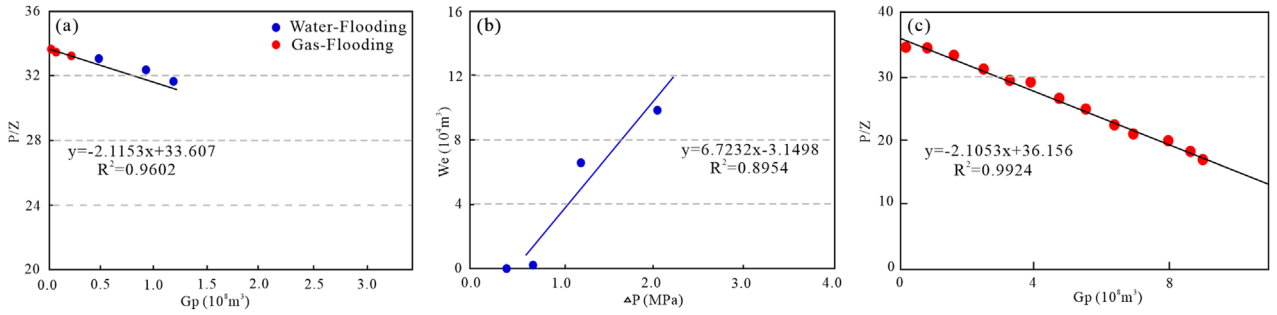

FIGURE 8
Pressure drawdown curve and water invasion: **(a)** Pressure drawdown curve of the HU2 well; **(b)** Water invasion curve of the HU2 well; **(c)** Pressure drawdown curve of the HU2006 well.

water invasion front advancing 978 m and a pore volume reduction of 356 × 10^4 m^3. In the eastern zone, the distance from the gas-water contact to Well HU2004 changed from 278.0 m to 238.0 m, with the water invasion front advancing only 40 m. Although water invasion occurred in $E_{1\text{-}2Z2}^{1}$, the gas saturation at the reservoir edges decreased, but the internal gas saturation basically remained unchanged. In addition, the upper main layers 1–6 ($E_{1\text{-}2Z2}^{1\text{-}1\text{-}1}$ to $E_{1\text{-}2Z2}^{1\text{-}2\text{-}2}$) were essentially unaffected by water invasion. In the $E_{1\text{-}2Z2}^{2}$ reservoir, bottom water intrusion occurred only locally in the eastern part (taking small layer 12 as an example), with the gas-water contact advancing 40 m (Figures 9c,d) and an average vertical rise of about 10.0 m (Figures 9e,f), indicating a limited affected range.

5.2.2 Injection-production stage water invasion characteristics

Seven-cycle injection-production numerical simulation was conducted to obtain the advancement of the gas-water front and changes in gas saturation for two sets of injection layer systems. A comprehensive analysis of the displacement characteristics of multiple injection-production cycles for the two injection systems is as follows:

1. In the $E_{1\text{-}2Z2}^{1}$ reservoir, water invasion mainly occurred in the lower main layers 7–11 ($E_{1\text{-}2Z2}^{1\text{-}2\text{-}2}$ to $E_{1\text{-}2Z2}^{1\text{-}2\text{-}4}$, Figures 10a,b), showing regional differences (taking small layer 7 as an example): In the western area, gas breakthrough at the water-front led to an increase in gas saturation, and the gas-drive expansion was significant but uneven (Figures 10c,d); in the eastern area, during high-rate injection-production, influenced by formation heterogeneity and differences in gas-water flow capacity, local gas fingering occurred, and gas saturation increased southeast of Well HUK1 (Figures 10e,f).
2. In the $E_{1\text{-}2Z2}^{2}$ reservoir, compared to before the USG construction (taking small layer 12 as an example), the gas-drive expansion effect was significant at the horizontal well toe and in the fracture zone north of Well HU001, and the gas saturation in the edge transition zone increased (Figures 10g,h).

5.3 The controlling factors of water invasion characteristics in the USG

5.3.1 Constraint of aquifer energy on water invasion scale

The aquifer energy of the Hutubi USG imposes a dual constraint on the scale of water invasion: 1) the aquifer size directly limits the total water influx (Fang et al., 2019). The static volumetric method estimated the affected volume of water invasion to be 7.93 × 10^8 m^3. However, numerical simulation indicates that the actual cumulative invaded water volume is only 50.2 × 10^4 m^3, accounting for merely 7.9% of the gas-filled pore volume. Moreover, the aquifer multiple (5 times) is significantly lower than that of strong water-drive reservoirs (typically >20 times), suggesting a small peripheral aquifer with strong sealing capacity. 2) The low activity of aquifer energy leads to discontinuous water invasion (Fang et al., 2024). After 2006, the pressure drawdown curve returned to a constant volume behavior, and the driving mechanism shifted from elastic water drive (B = 1.85) to constant volume depletion (B→ ∞). The water drive index is only 0.025, indicating an interruption of aquifer recharge and weak driving force, resulting in selective regional water invasion and localized bottom-water coning rather than large-scale areal expansion.

5.3.2 Control of reservoir characteristics and spatial distribution on water invasion pathways

The water invasion characteristics of the Hutubi UGS are governed by a dynamic coupling of "structure–deposition–reservoir properties–heterogeneity". A regional reverse fault on the southern side (fault displacement >100 m, SGR >0.65) forms a rigid boundary that seals the southern aquifer, resulting in edge water being mainly distributed on the eastern, western, and northern flanks of the $E_{1\text{-}2Z2}^{1}$ reservoir. The main body of the $E_{1\text{-}2Z2}^{1}$ reservoir develops underwater distributary channels and mouth bars, while the low-lying areas to the east, west, and north are dominated by sheet sands deposited between distributary channels and mud-rich siltstones, forming medium-to low-permeability layers with poorer continuity than the main reservoir. This results in three-sided low-permeability sealing, with a permeability gradient difference of 3.2 times along the NE-SW direction, effectively limiting the extent of edge water (cumulative invaded water volume of 50.2

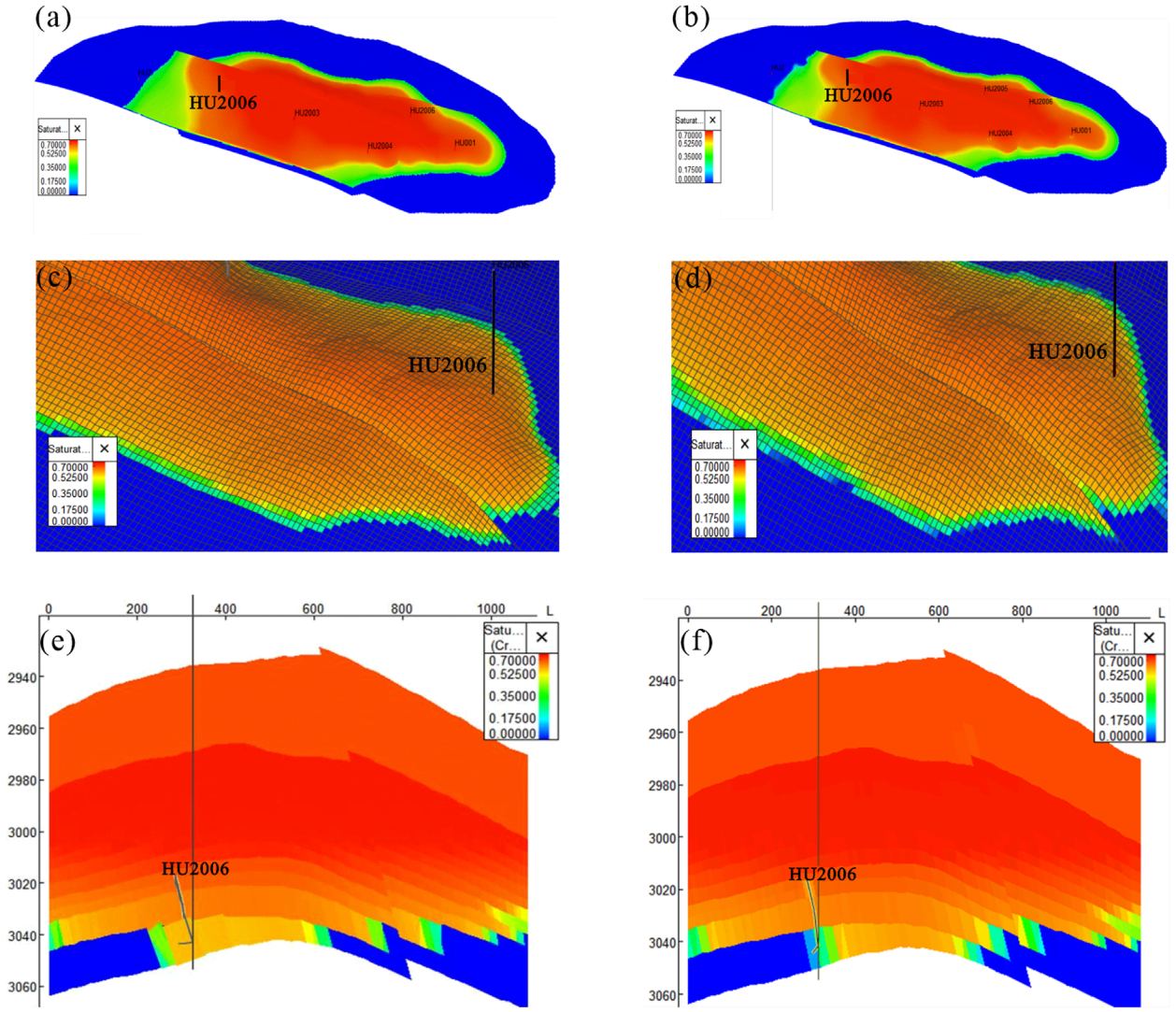

FIGURE 9
The water invasion characteristics of the second member of the Paleogene Ziniquanzi Formation sandstone from the Hutubi gas storage before and at the end of development: **(a,b)** The water invasion characteristics of the seventh layer of $E_{1\text{-}2Z2}^{1}$ gas reservoir before and at the end of development; **(c,d)** The water invasion characteristics of the 12th layer in the eastern area of $E_{1\text{-}2Z2}^{2}$ gas reservoir before and at the end of development; **(e,f)** The vertical water saturation diagram of well HU2006 in $E_{1\text{-}2Z2}^{2}$ gas reservoir before and after development.

$\times 10^4$ m^3). As the production degree increases, the formation pressure drops, and the western structural low (−3,051.0 m) coupled with high-permeability zones (>60 mD) drives orderly inward advancement of the aquifer, while the eastern uplifted structure (no water breakthrough at Well Hu001) forms a natural barrier to water invasion. Strong intra- and interlayer heterogeneity (permeability contrast >1,000) causes vertical differentiation of water invasion, with only the lower part of the $E_{1\text{-}2Z2}^{1\text{-}2}$ sublayer and local zones of the $E_{1\text{-}2Z2}^{2}$ reservoir affected (Figures 10a,b). In terms of planar distribution, a 24-fold difference in water invasion advancement is observed (978 m westward vs. 40 m eastward), controlled by spatial property variations (high-permeability zones concentrated in the west). Gas expansion response is evident in high-permeability areas under injection-production disturbances. The coupling of reservoir properties and structural features results in contrasting behaviors: although the bottom-water of the $E_{1\text{-}2Z2}^{2}$ reservoir exhibits high permeability (>60 mD), water invasion is constrained by structural closure (only −10 m interface uplift), whereas the combination of the structural depression and high-permeability channels in the western $E_{1\text{-}2Z2}^{1}$ reservoir forms preferential water invasion pathways (from Well Hu2 to Well Hu 2002, with the water-gas ratio increasing westward and decreasing eastward). The interaction of these four-dimensional elements forms a dynamic coupling mechanism of "structural sealing–depositional control on flow–heterogeneity-induced differentiation–property selection" (Li et al., 2022; Guo et al., 2024)resulting in westward-directed water invasion ($E_{1\text{-}2Z2}^{1}$), localized bottom-water coning ($E_{1\text{-}2Z2}^{2}$), and heterogeneous planar expansion, with the cumulative water invasion volume accounting for only 7.9% of the gas-filled pore volume.

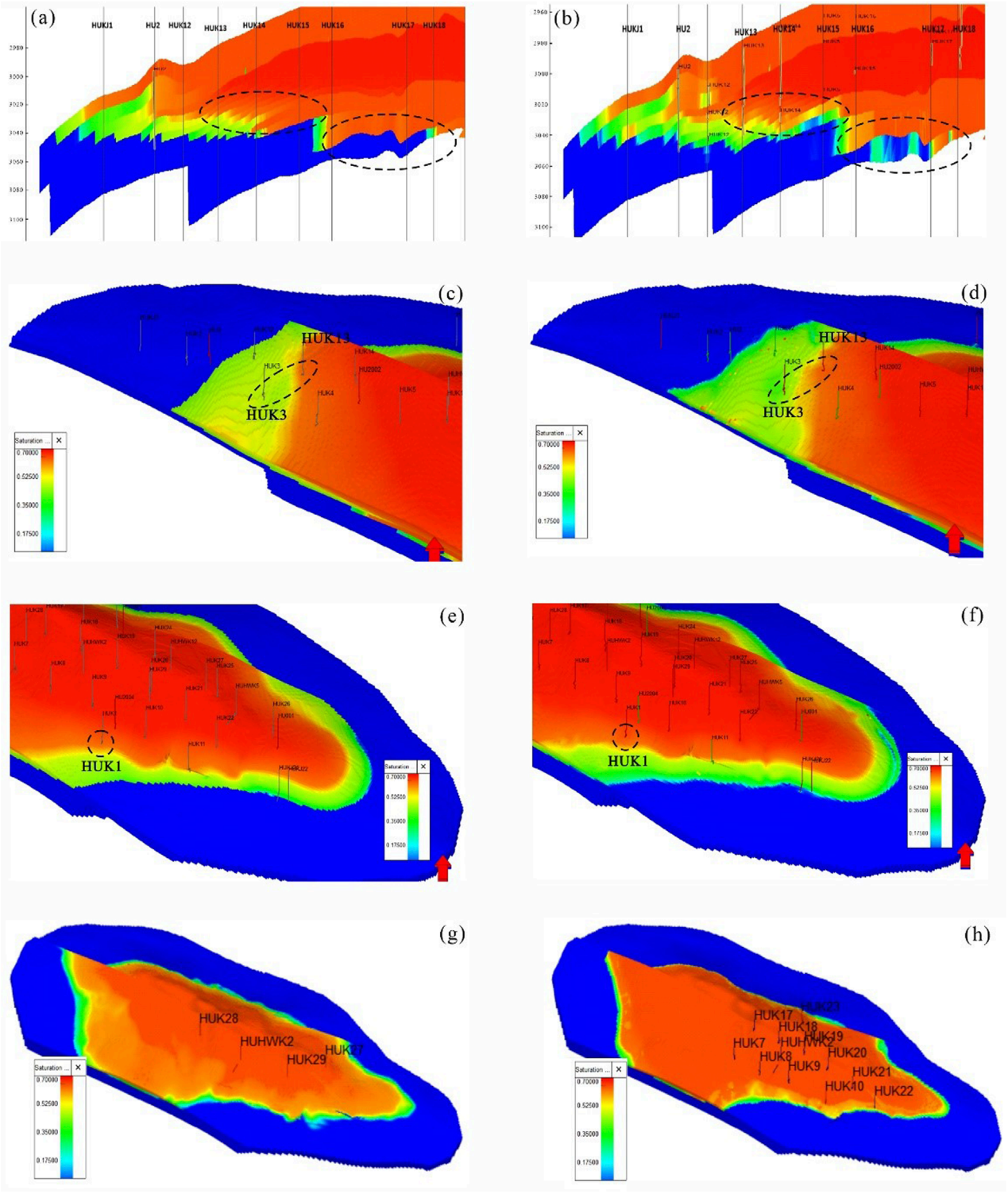

FIGURE 10
The water invasion characteristics of the second member of the Paleogene Ziniquanzi Formation sandstone from the Hutubi gas storage at the end of development and the seventh cycle of gas production: **(a,b)** The water invasion characteristics in the western area of E1-2z21 gas reservoir at the end of development and the seventh cycle of gas production; **(c,d)** The water invasion characteristics of the 7th layer in the western area of E1-2z21 gas reservoir at the end of development and the seventh cycle of gas production; **(e,f)** The water invasion characteristics of the 7th layer in the eastern area of E1-2z21 gas reservoir at the end of development and the seventh cycle of gas production; **(g,h)** The water invasion characteristics of the 12th layer of E1-2z22 gas reservoir at the end of development and the seventh cycle of gas production.

5.3.3 Aggravation of gas–water locking by reservoir petrography and pore structure

The dynamic behavior of water invasion under strong injection–production conditions in the UGS fundamentally differs from that of conventional gas reservoirs (Tang et al., 2021). During the injection phase, high-pressure gas displaces edge water outward at high velocities, rapidly increasing formation pressure. Although gas storage capacity expands, the water invasion volume is suppressed due to the reduced pressure differential. Conversely, during the production phase, the gas withdrawal rate is ten times that of conventional reservoirs, causing a sharp pressure drop that triggers reverse water influx, leading to a rapid decrease in gas storage capacity and an exponential increase in water invasion volume (Zhu et al., 2021). This cyclical pressure fluctuation causes repeated reversals in the direction of gas–water two-phase migration within the reservoir, significantly amplifying the effects of heterogeneity (Liu et al., 2022). Given that permeability contrasts can reach 10-100 times, high-permeability zones under strong injection–production form high-velocity flow channels, with flow rates exceeding Darcy flow limits (Reynolds number >1), inducing inertial effects and turbulent flow. Meanwhile, low-permeability layers remain poorly mobilized, with most pore space becoming "ineffective storage," further widening the utilization gap between high- and low-permeability zones.

Additionally, differences in microscopic pore structures directly govern the heterogeneity of water invasion (Peng et al., 2024). In the central zone, large pore throats dominate flow, resulting in good pore connectivity, high mobilization efficiency, and continuous alternating gas–water flow, thereby maintaining stable internal gas saturation. In contrast, the western and eastern zones exhibit fine pore throats, which cause significant capillary resistance, intensifying gas–water locking and reducing gas recoverability. When gas and water phases migrate through fine pore structures, the gas phase tends to become trapped, forming three types of trapped gas: bypassed gas, snap-off gas, and water-locked gas (Singh et al., 2017). Under low displacement pressure differentials dominated by capillary forces, the water phase preferentially invades small throats and rapidly breaks through, while gas is bypassed and trapped in larger throats due to lower capillary forces and slower flow (Figure 11a). Under high displacement pressure differentials dominated by hydrodynamic forces, the water phase preferentially occupies larger throats, leaving gas stranded in smaller throats due to higher flow resistance (Figure 11b) (Hu et al., 2021; Chu et al., 2024). Pore–throat scale effects further exacerbate gas entrapment. Narrow throats induce additional resistance due to the Jamin effect, and continuous water films form along hydrophilic pore walls (He et al., 2021). As gas passes through, it undergoes deformation, contraction, and expansion cycles leading to snap-off events (Figure 11c). Although accumulated energy from bubble collisions may temporarily restore flow, gas ultimately becomes dispersed into isolated bubbles (Xiong et al., 2024). Water-locking gas arises from capillary suction compressing gas flow paths, forming localized closures (Figure 11d) (Jiang et al., 2024).

The spatial distribution of different gas-locking types exhibits clear heterogeneity. Bypassed gas commonly develops in peripheral low-permeability zones, where fine pore throats and strong capillary forces allow water to preferentially invade narrow channels and rapidly break through, while gas in larger pores with weaker capillary control and slower displacement becomes isolated. These peripheral zones often align with the direction of aquifer advance, leading to continuous accumulation of bypassed gas along invasion pathways and forming banded stratigraphic patterns. Snap-off and residual trapping mainly occur within wellbores and adjacent injection–production disturbance zones. Under high displacement pressures, water preferentially enters large pores, generating high-velocity flow, while gas in fine throats undergoes deformation, contraction, and expansion under the combined influence of the Jamin effect and water-film formation, ultimately resulting in snap-off or retention. Consequently, trapped gas in these near-well zones tends to cluster in point–band composites. Water-blocked gas is typically associated with mudstone interbeds or fine-grained intervals, where hydrophilic pore walls promote capillary imbibition that compresses gas flow channels, producing locally confined clusters with a vertically stratified distribution. Overall, the structural high in the central anticline, with coarser throats and better connectivity, allows more continuous gas flow and weaker locking effects during water invasion. In contrast, reservoir margins and fine-pore-throat domains, characterized by higher capillary pressures and restricted flow channels, are more prone to multiple gas-locking mechanisms and thus represent the primary zones of trapped-gas accumulation.

5.4 Engineering implications

Based on a systematic analysis of reservoir architecture, water-invasion response, and pore–throat characteristics, this study establishes a coupled control mechanism of "aquifer-driven capacity, structural boundary sealing, facies-guided transport, heterogeneity-induced differentiation, petrophysical channel selection, and pore-scale gas locking." This framework reveals the spatial heterogeneity of water-invasion behavior under the combined influence of multi-scale factors and provides the following engineering guidance for UGS operations:

Optimization of injection–production schemes: In the western zone, proximity to the aquifer source, structural lows, and strong connectivity result in pronounced water-invasion responses. It is therefore recommended to reduce injection–withdrawal pressure differentials and optimize cycle frequency and intensity to suppress rapid aquifer front advancement. In contrast, the eastern zone is characterized by dense fault development with strong lateral sealing capacity, allowing a relatively more flexible injection–production regime to maximize gas withdrawal efficiency.

Identification and fine-tuned regulation of high-risk gas-locking zones: Different types of gas locking (e.g., bypassed, snapped-off, and water-blocked gas) show significant spatial clustering in the low-permeability flanks and locally poorly connected sectors of the central zone. It is advisable to delineate these high-risk zones through pore–throat analysis and numerical simulation, followed by well-level pressure control, tailored injection–production adjustments, or zonal/stratified management to mitigate the adverse impact of gas locking on effective recovery.

Establishment of a multi-parameter reservoir zoning evaluation system: By integrating structural boundaries, sedimentary distribution, petrophysical variations, and gas-locking types, a refined reservoir zoning model can be constructed. This enables

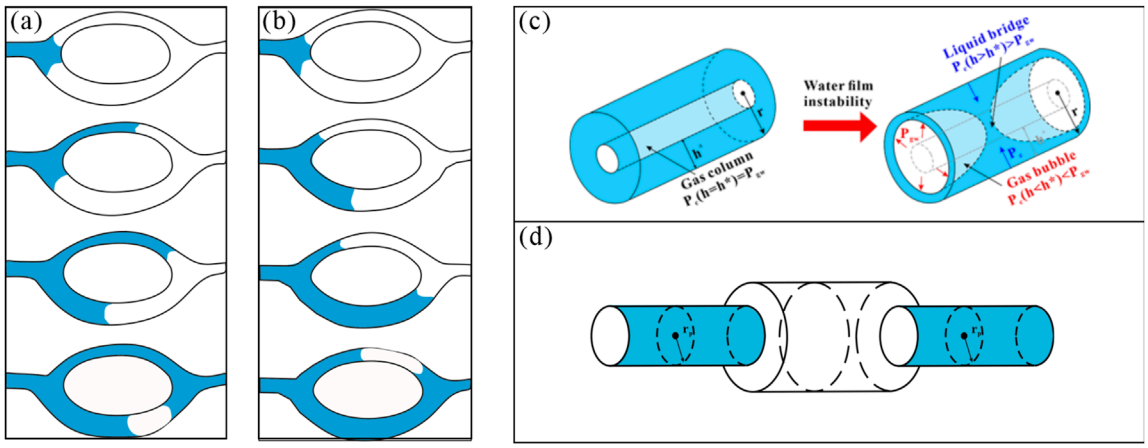

FIGURE 11
Microscopic pore structure aggravates gas-water interlocking schematic diagram: **(a)** The trapped gas at low pressure; **(b)** The trapped gas at high pressure; **(c)** The cut gas; **(d)** The water-locked gas.

precise identification of invasion pathways, gas-locking-prone areas, and low-efficiency well intervals, thereby supporting zonal optimization of injection–production regimes and targeted recovery of residual gas.

In summary, the proposed six-factor coupled mechanism not only advances understanding of water-invasion and gas-locking behavior in UGS but also provides a practical and operable framework for dynamic regulation and differentiated management of structurally complex storage reservoirs, offering substantial engineering applicability and scalability.

6 Conclusion

This study conducted a comprehensive evaluation of the aquifer energy, water invasion dynamics, and their controlling factors in the Hutubi Gas Storage under strong injection–production conditions, yielding the following key findings:

1. The aquifer multiple remains stable at approximately 5, with a cumulative water invasion volume of around 50.2×10^4 m^3, accounting for less than 12% of the gas-bearing pore volume. The calculated water drive index is merely 0.025, conclusively verifying that the second member of the Ziniquanzi Formation in the Hutubi Gas Storage constitutes a weak water-drive reservoir characterized by limited and inactive aquifer energy.
2. The water invasion behavior of the second member of the Ziniquanzi Formation exhibits pronounced layer selectivity and directionality. Water invasion in the $E_{1\text{-}2Z2}^{1}$ reservoir primarily occurs in the lower sublayers ($E_{1\text{-}2Z2}^{1\text{-}2\text{-}2}$ to $E_{1\text{-}2Z2}^{1\text{-}2\text{-}4}$) and displays significant regional heterogeneity. During the production phase, the water invasion front advanced 978 m in the western area but only 40 m in the east. During multiple injection–production cycles, gas saturation in the transitional zones at the edges of the east and west increased, indicating gas-driven expansion phenomena, albeit unevenly. In the $E_{1\text{-}2Z2}^{2}$ reservoir, localized bottom water breakthrough was observed during the production phase (gas–water interface uplifted by 10 m), while during the injection–production cycles, significant gas-driven expansion occurred at horizontal well tips and fault zones, although the overall influence of the aquifer remained limited without compromising the stability of internal gas saturation.
3. The water invasion behavior in the second member of the Ziniquanzi Formation is controlled by a dynamic coupling mechanism involving "aquifer–structure–deposition–heterogeneity–reservoir properties–microscopic pore structure". Specifically:
    1. The scale and energy of the aquifer jointly constrain the total amount and continuity of water invasion;
    2. A regional reverse fault (>100 m displacement) effectively blocks southern aquifer encroachment, while coupling between the western structural low (−3,051.0 m) and high-permeability belts (>60 mD) drives the inward advance of the water front;
    3. Strong intra- and interlayer heterogeneity (permeability variation coefficient >1.3) causes vertical differentiation of water invasion; Planar heterogeneity (with a 24-fold difference in advance distance between west and east) results in directional expansion of the water invasion front;
    4. Under injection–production disturbances, gas saturation in high-permeability zones increased by 15%–20%;
    5. Microscopic pore–throat effects (bypass trapping, snap-off, and water-locking) lead to residual gas accumulation, causing ineffective pore volume in low-permeability zones.

These findings provide critical geological insights and technical references for the efficient development and management of similar gas storage projects operating under strong injection–production regimes.

Data availability statement

Data will be made available on request.

Author contributions

WL: Methodology, Funding acquisition, Project administration, Investigation, Writing – review and editing. SZ: Writing – review and editing, Investigation, Methodology. ML: Methodology, Investigation, Writing – original draft, Data curation. YZ: Resources, Writing – review and editing, Project administration. HY: Investigation, Data curation, Writing – original draft. GS: Data curation, Writing – original draft, Investigation. MN: Methodology, Writing – review and editing. LM: Writing – review and editing, Methodology. MS: Methodology, Writing – review and editing. ZS: Methodology, Investigation, Writing – original draft, and Data curation.

Funding

The author(s) declare that financial support was received for the research and/or publication of this article. This research was supported by the National Foreign Expert Project of the Ministry of Human Resources and Social Security of China (AI-Driven Theories and Technologies for Geological Carbon Dioxide Sequestration, H20240336); the 'Interdisciplinary Frontier Exploration Special Project' of China University of Petroleum (Beijing) (Composite Hydrocarbon Generation Mechanism and Resource Potential in Ultra-/Super-Deep Layers of Western China, 2462024XKQY001); the Tianshan Elite Program – Young Top-Talent Support Project of the Xinjiang Uygur Autonomous Region (2024TSYCJC0008); and PetroChina Xinjiang Oilfield Company (Research on the Reservoir Space Utilization Mechanism of Hutubi Gas Storage, HTBCQK-2024-130).

Acknowledgments

We would also thank Hutubi Gas Storage Company PetroChina Xinjiang Oilfield Company for providing core samples and necessary data.

Conflict of interest

Authors WL, SZ, and YZ were employed by Xinjiang Oilfield Gas Storage Co., Ltd, PetroChina.

The remaining authors declare that the research was conducted in the absence of any commercial or financial relationships that could be construed as a potential conflict of interest.

The authors declare that this study received funding from PetroChina Xinjiang Oilfield Company. The funder had the following involvement in the study: study design, data collection, data analysis, decision to publish and preparation of the manuscript.

The author(s) declared that they were an editorial board member of Frontiers, at the time of submission. This had no impact on the peer review process and the final decision.

Correction note

A correction has been made to this article. Details can be found at: 10.3389/feart.2025.1717287.

Generative AI statement

The author(s) declare that no Generative AI was used in the creation of this manuscript.

Any alternative text (alt text) provided alongside figures in this article has been generated by Frontiers with the support of artificial intelligence and reasonable efforts have been made to ensure accuracy, including review by the authors wherever possible. If you identify any issues, please contact us.

Publisher's note

All claims expressed in this article are solely those of the authors and do not necessarily represent those of their affiliated organizations, or those of the publisher, the editors and the reviewers. Any product that may be evaluated in this article, or claim that may be made by its manufacturer, is not guaranteed or endorsed by the publisher.

References

Agarwal, R. G. (1967). *Unsteady-state performance of water-drive gas reservoirs. PhD dissertation*. United States: Texas A&M University.

Al-Shafi, M., Massarweh, O., Abushaikha, A. S., and Bicer, Y. (2023). A review on underground gas storage systems: natural gas, hydrogen and carbon sequestration. *Energy Rep.* 9, 6251–6266. doi:10.1016/j.egyr.2023.05.236

Chen, P. Y., Liu, H. Q., Zhao, H. L., Guo, C. Q., Xing, Y. Z., Cheng, M. W., et al. (2021). Microscopic characteristics of water invasion and residual gas distribution in carbonate gas reservoirs. *Energy Sci. and Eng.* 9, 2151–2164. doi:10.1002/ese3.972

Chen, D., Zhang, C. Z., Yang, M., Li, H. M., Wang, C. L., Diwu, P. X., et al. (2024). Research on water invasion law and control measures for ultradeep, fractured, and low-porosity sandstone gas reservoirs: a case study of kelasu gas reservoirs in tarim basin. *Processes* 12 (2), 310. doi:10.3390/pr12020310

Cheng, H., Jiang, L., and Li, C. G. (2022). Experimental study on production characteristics of bottom water fractured-vuggy reservoir. *Geofluids* 2022, 1–22. doi:10.1155/2022/7456697

Chu, H. T., Zhang, J. C., Cao, Y. X., Li, X. L., Yu, H. Y., Li, F. X., et al. (2024). Water invasion and residual gas distribution in partially filled fractures *via* phase-field method. *Phys. Fluids* 36 (11), 112032. doi:10.1063/5.0236093

Ding, G. S. (2010). Developing trend and motives for global underground gas storage. *Nat. Gas. Ind.* 30 (8), 59–61+117. doi:10.3787/j.issn.1000-0976.2010.08.016

Fang, F. F., Shen, W. J., Li, X. Z., Gao, S. S., Liu, H. X., and Li, J. (2019). Experimental study on water invasion mechanism of fractured carbonate gas reservoirs in longwangmiao formation, moxi block, sichuan basin. *Environ. Earth Sci.* 78, 316. doi:10.1007/s12665-019-8325-x

Fang, F. F., He, S. J., Zhuang, J., Zhang, J., and Bian, Y. N. (2024). Large-scale physical simulation experiment of water invasion law for multi-well development in sandstone gas reservoirs with strong water drive. *Appl. Sci.* 14 (17), 8067. doi:10.3390/app14178067

Feng, X., Zhong, B., Yang, X. F., and Deng, H. (2015). Effective water influx control in gas reservoir development: problems and countermeasures. *Nat. Gas. Ind.* 35 (2), 35–40. doi:10.1016/j.ngib.2015.07.016

Guo, P., Zheng, J., Dong, C., Wang, Z. H., Liao, H. G., and Fan, H. J. (2024). Invasion characteristics of marginal water under the control of high-permeability zones and its influence on the development of vertical heterogeneous gas reservoirs. *Energies* 17 (18), 4724. doi:10.3390/en17184724

Han, X. B., Tan, X. H., Li, X. P., Kui, M. Q., Meng, Z., Zhao, Z. H., et al. (2022). A water invasion unit numerical simulation model for the distribution of water and water invasion channel in complex edge water reservoir. *J. Petroleum Sci. Eng.* 215, 110508. doi:10.1016/j.petrol.2022.110508

Han, D. H., Xiong, W., Jiang, T. W., Gao, S. S., Liu, H. X., Ye, L. Y., et al. (2023). Investigation of the water-invasion gas efficiency in the Kela-2 gas field using multiple experiments. *Energies* 16 (20), 7216. doi:10.3390/en16207216

He, M. X., Zhou, Y. F., Wu, K. L., Hu, Y. L., Feng, D., Zhang, T., et al. (2021). Pore network modeling of thin water film and its influence on relative permeability curves in tight formations. *Fuel* 289, 119828. doi:10.1016/j.fuel.2020.119828

Holtz, M. H., and Major, R. P. (2004). Integrated geological and petrophysical characterization of Permian shallow-water dolostone. *SPE Reserv. Eval. and Eng.* 7 (1), 47–58. doi:10.2118/89090-PA

Hu, Y., Li, X. Z., Shen, W. J., Guo, C. M., Jiao, C. Y., Xu, X. X., et al. (2021). Study on the water invasion and its effect on the production from multilayer unconsolidated sandstone gas reservoirs. *Geofluids* 2021, 1–9. doi:10.1155/2021/5135159

Hu, J. T., Yang, S. L., Jiang, Y., Deng, H., Wang, M. Y., You, L., et al. (2024). Experimental study on edge water invasion of strongly heterogeneous carbonate gas reservoirs based on NMR technology. *Processes* 12 (7), 1361. doi:10.3390/pr12071361

Huang, S. J., He, X. L., Xu, J. J., Zhang, X. J., Fan, J., Yang, X. P., et al. (2015). An evaluation method of water influx for reconstructing gas storage in condensate gas reservoir. *Oil Gas Storage Transp.* 34 (2), 154–157. doi:10.6047/j.issn.1000-8241.2015.02.008

Huang, K., Huang, S. Y., Jiang, Q., Gates, I. D., and Fan, D. (2025a). Analytical prediction model for edge water invasion flow rate in SAGD heavy oil reservoirs. *Geoenergy Sci. Eng.* 244, 213404. doi:10.1016/j.geoen.2024.213404

Huang, K., Huang, S. Y., Wang, Z. Y., Wang, G. D., Jiang, Q., Gates, I. D., et al. (2025b). Mechanism evaluation of edge-water invasion mitigation by low temperature oxidation (LTO) coking in VHSD heavy oil reservoirs: a comparative study with traditional plugging techniques. *Fuel* 382, 133801. doi:10.1016/j.fuel.2024.133801

Jiang, T. W., Qi, H., Wang, Z. M., Li, Y. Q., Wang, J. F., Liu, Z. Y., et al. (2024). Microscopic experiment on efficient construction of underground gas storages converted from water-invaded gas reservoirs. *Petroleum Explor. Dev.* 51, 203–212. doi:10.1016/S1876-3804(24)60017-0

Keelan, D. K. (1976). A practical approach to determination of imbibition gas-water relative permeability. *J. Petroleum Technol.* 28 (2), 199–204. doi:10.2118/4988-pa

Li, X., Fu, X. H., Tian, J., Guan, W. M., Liu, X. L., Ge, Y. Y., et al. (2019). Heterogeneities of seepage pore and fracture of high volatile bituminous coal core: implications on water invasion degree. *J. Petroleum Sci. Eng.* 183, 106409. doi:10.1016/j.petrol.2019.106409

Li, P. Y., Cheng, C., Ruan, J. F., Luo, H., Li, W. S., Ye, Y., et al. (2022). Gas–water distribution pattern of large-scale low and gentle structure gas reservoirs — a case study of the longwangmiao formation gas reservoir in MX gas field in sichuan Basin. *Desalination Water Treat.* 268, 254–263. doi:10.5004/dwt.2022.28697

Li, H. T., Yu, G., Li, C., Xie, Z. L. ;., Liu, C. X., Zhang, D. M., et al. (2023a). Prediction model and risk quantification of natural gas peak production in central sichuan paleo-uplift gas reservoirs. *Geofluids* 2023, 1–15. doi:10.1155/2023/4858118

Li, Y. D., You, Y. C., Zeng, D. Q., Shi, Z. L., Gu, S. H., and Zhang, R. (2023b). Numerical simulation of water intrusion in wet gas reservoirs: a case study of the changxing gas reservoir in yuanba. *Earth Sci. Front.* 30 (6), 341–350. doi:10.13745/j.esf.sf.2023.2.26

Liu, H. X., Gao, S. S., Ye, L. Y., Zhu, W. Q., and An, W. G. (2020). Change laws of water invasion performance in fractured-porous water-bearing gas reservoirs and key parameter calculation methods. *Nat. Gas. Ind.* 40 (6), 90–99.

Liu, T., Li, Y. Q., Ding, G. S., Wang, Z. M., Shi, L., Liu, Z. Y., et al. (2022). Simulation of pore space production law and capacity expansion mechanism of underground gas storage. *Petroleum Explor. Dev.* 49 (6), 1423–1429. doi:10.1016/S1876-3804(23)60360-X

Liu, Z. L., Chen, D., Gao, Z. Y., Wu, Y. P., Zhang, Y. Z., Fan, K. Y., et al. (2023a). 3D geological modeling of deep fractured low porosity sandstone gas reservoir in the kuqa depression, tarim basin. *Front. Earth Sci.* 11, 1171050. doi:10.3389/feart.2023.1171050

Liu, Q. M., Tang, H. F., Lv, Z. K., Wang, Q. F., Liu, Z. L., and Chang, B. H. (2023b). Study on gas–water distribution and water invasion law under different fracture development models in ultra-deep gas reservoir: taking keshen 2, 9 and 8 gas reservoirs of tarim basin as examples. *Nat. Gas. Geosci.* 34 (6), 963–972. doi:10.3389/feart.2023.1171050

Ma, Y. Q., Liu, B. L., Liu, X. L., Wu, C. W., Pei, S., Chen, Y. K., et al. (2023). Water invasion prediction method for edge–bottom water reservoirs: a case study in an oilfield in Xinjiang, China. *Processes* 11 (3), 919. doi:10.3390/pr11030919

Mao, W. Z., Yao, Y. J., Qin, Z., Liu, Y. D., Han, J. H., and Liu, Z. (2024). Pore structure characterization of sandstone under different water invasion cycles using micro-CT. *Geomechanics Geophys. Geo-Energy Geo-Resources* 10 (1), 53. doi:10.1007/s40948-023-00696-z

Pan, Z. Q., Jin, Z. J., Li, G. S., and Zhang, K. Q. (2024). Assessing subsurface gas storage security for climate change mitigation and energy transition. *Geophys. Res. Lett.* 51, e2024GL109913. doi:10.1029/2024GL109913

Patacchini, L. (2017). Peripheral water injection efficiency for material balance applications. *J. Petroleum Sci. Eng.* 149, 720–739. doi:10.1016/j.petrol.2016.10.032

Peng, X., Hu, Y. H., Zhang, F., Zhang, R. H., and Zhao, H. G. (2024). A review on the water invasion mechanism and enhanced gas recovery methods in carbonate bottom-water gas reservoirs. *Processes* 12 (12), 2748. doi:10.3390/pr12122748

Ren, Z. X., Yang, X. P., Chang, D. W., Wang, N., and Meng, D. (2024). Study of the effect of salt deposition on production capacity and storage capacity in underground gas storage. *Front. Earth Sci.* 12, 1362776. doi:10.3389/feart.2024.1362776

Shi, Q. D., Wang, Y., Jvlaiti, S. M. Y., Shi, X. P., Liao, W., Li, C., et al. (2012). Distribution of formation water and analysis of water invasion pattern in hutubi gas field. *Xinjiang Pet. Geol.* 33 (4), 479–480.

Singh, K., Menke, H., Andrew, M., Lin, Q. Y., Rau, C., Blunt, M. J., et al. (2017). Dynamics of snap-off and pore-filling events during two-phase fluid flow in permeable media. *Sci. Rep.* 7, 5192. doi:10.1038/s41598-017-05204-4

Song, Z. Z., Lv, M. Y., Zhao, L. B., Liu, C. Q., He, Y. Y., Zhang, Y. Q., et al. (2024). A novel bound water occurrence model for tight sandstone. *Fuel* 357, 130030. doi:10.1016/j.fuel.2023.130030

Tan, X. H., Han, X. B., Li, X. P., Meng, Z., Zhang, F., Li, L. X., et al. (2025). Modeling the water transport in water invasion channel with water invasion unit numerical simulation based on intelligent proxies. *Phys. Fluids* 37 (2), 023330. doi:10.1063/5.0252355

Tang, L. G., Wang, J. M., Bai, F. J., and Shi, L. (2014). Inventory forecast of underground gas storage based on modified material balance equation. *Petroleum Explor. Dev.* 41, 528–532. doi:10.1016/S1876-3804(14)60062-8

Tang, L. L., Lu, Z., Zhang, M., Sun, L., and Wen, L. X. (2018). Seismicity induced by simultaneous abrupt changes of injection rate and well pressure in hutubi gas field. *J. Geophys. Res. Solid Earth* 123, 5929–5944. doi:10.1029/2018JB015863

Tang, Y., Long, K. J., Wang, J. M., Xu, H. C., Wang, Y., He, Y. W., et al. (2021). Change of phase state during multi-cycle injection and production process of condensate gas reservoir based underground gas storage. *Petroleum Explor. Dev.* 48 (2), 395–406. doi:10.1016/S1876-3804(21)60031-9

Xiong, Y., Fu, X. T., Feng, P. X., Zhao, Z. H., Jiang, J., and Fu, H. H. (2024). Microscopic occurrence of primary water in carbonate gas reservoirs with fractures and vugs and its effect on water invasion mechanism. *J. Hydrology* 635, 131087. doi:10.1016/j.jhydrol.2024.131087

Xu, X., Li, X. Z., Hu, Y., Mei, Q. Y., Shi, Y., and Jiao, C. Y. (2021). Physical simulation for water invasion and water control optimization in water drive gas reservoirs. *Sci. Rep.* 11, 6301. doi:10.1038/s41598-021-85548-0

Yang, Y., Xia, S. Y., Huang, P., and Qian, J. X. (2024). Energy transition: connotations, mechanisms and effects. *Energy Strategy Rev.* 52, 101320. doi:10.1016/j.esr.2024.101320

Yao, C., Yan, R. F., Zhou, F., Zhang, Q., Niu, G., Chen, F. F., et al. (2024). A novel method to calculate water influx parameters and geologic reserves for fractured-vuggy reservoirs with bottom/edge water. *Energies* 17 (12), 2822. doi:10.3390/en17122822

Zeren, F., and Akkuş, H. T. (2020). The relationship between renewable energy consumption and trade openness: new evidence from emerging economies. *Renew. Energy* 147, 322–329. doi:10.1016/j.renene.2019.09.006

Zhang, G. X., Li, B., Zheng, D. W., Ding, G. S., Wei, H., Qian, P. S., et al. (2017). Challenges to and proposals for underground gas storage (UGS) business in China. *Nat. Gas. Ind. B* 4, 231–237. doi:10.1016/j.ngib.2017.07.025

Zhang, B., Song, L. L., Ji, Z. B., Wang, B. S., and Wu, Z. D. (2020). Progress and prospect of geophysical research on underground gas storage: a case study of hutubi gas storage, Xinjiang, China. *Earthq. Res. China* 34 (2), 187–209. doi:10.19743/j.cnki.0891-4176.202002006

Zhang, R. H., Chen, S. N., Hu, S. Y., Zhao, Y. L., Zhang, B. N., and Wang, R. H. (2021). Numerical simulation and laboratory experiments of CO_2 sequestration and being as cushion gas in underground natural gas storage reservoirs. *J. Nat. Gas Sci. Eng.* 85, 103714. doi:10.1016/j.jngse.2020.103714

Zhang, P. J., Fan, H. R., Wen, G. Y., Mu, L. Y., Cheng, W. H., Wang, X. C., et al. (2024). A new workflow for warning and controlling the water invasion. *J. Petroleum Explor. Prod. Technol.* 14, 2089–2099. doi:10.1007/s13202-024-01812-9

Zheng, D. W., Wanyan, Q. Q., and Zhao, K. (2025). Development status and prospect of underground natural gas storage in China. *Int. Pet. Econ.* 33 (7), 37–45. doi:10.3969/j.issn.1004-7298.2025.07.005

Zhi, Jq., Bo, Lf., Qu, Gh., Jiang, N., and Zhang, R. Z. (2022). Water invasion law and water invasion risk identification method for deep sea bottom-water gas reservoir. *Energies* 15 (5), 1937. doi:10.3390/en15051937

Zhu, S. N., Sun, J. C., Wei, G. Q., Zheng, D. W., Wang, J. M., Shi, L., et al. (2021). Numerical simulation-based correction of relative permeability hysteresis in water-invaded underground gas storage during multi-cycle injection and production. *Petroleum Explor. Dev.* 48 (1), 190–200. doi:10.1016/S1876-3804(21)60015-0

Zou, C. N., Ma, F., Pan, S. Q., Zhao, Q., Fu, G. Y., Zhang, G. S., et al. (2023). Global energy transition revolution and the connotation and pathway of the green and intelligent energy system. *Petroleum Explor. Dev.* 50, 722–740. doi:10.1016/S1876-3804(23)60423-9